Spatiotemporal Motifs of Cerebral Theta Oscillations in Freely Moving Mice

by

Nicholas James Sattler

A dissertation accepted and approved in partial fulfillment of the

requirements for the degree of

Doctor of Philosophy

in Biology

Dissertation Committee:

Shawn Lockery, Chair

Michael Wehr, Advisor

Cris Niell, Core Member

Philip Washbourne, Core Member

Michael Harms, Institutional Representative

University of Oregon

Spring 2024

DISSERTATION ABSTRACT

Nicholas James Sattler

Doctor of Philosophy in Biology

Title: Spatiotemporal Motifs of Cerebral Theta Oscillations in Freely Moving Mice

Mice are the most commonly used mammal in systems neuroscience, yet the ability to implement large-scale neural recordings and behavioral monitoring in freely moving conditions has remained methodologically challenging. Due to these difficulties, traditional methods resort to heavily restraining mice in “head-fixed conditions” to achieve stable recordings of neural activity and behavioral monitoring. Such practices, however, drastically restrict the flexibility of both their behavior and the neural activity intended to be studied in the first place. In freely moving conditions, movement-related activity across the cerebral cortex has been shown to be organized by theta oscillations. While there has been significant progress in the ability to simultaneously record from large numbers of neurons using calcium imaging and electrophysiological probes, our understanding of theta oscillations on global cortical function has similarly been stymied by these method’s shortcomings in temporal resolution and spatial scale respectively.

This dissertation aims to address these issues through the development and integration of new methodologies. In Chapter II, I present a novel head-mounted camera system for monitoring freely moving mice. The advantages of this system allow large-scale electrophysiological recordings to be paired with multi-camera headsets, enabling the ability to simultaneously record the fine movements of the eyes, ears, whiskers, nostrils, and visual field in freely moving

conditions. In Chapter III, I utilize these techniques to identify a distinct behavioral pattern of the nostrils and ears during freely moving mouse behavior. Additionally, through the development and integration of cortex-wide electrocorticography —a method of electrophysiology that records across large areas of the cortex at high spatiotemporal resolution— I also identify distinct cortex-wide spatiotemporal motifs of cerebral theta oscillations prominent during natural behavior. These novel findings open up new avenues of investigation for understanding how the brain integrates information into the production of ongoing behavior in natural conditions.

This dissertation includes previously published and unpublished co-authored material. This dissertation also includes seven supplementary videos related to the material described in Chapter II.

ACKNOWLEDGMENTS

I would like to thank the members of my committee Shawn Lockery, Cris Niell, Phil Washbourne, and Mike Harms for their time, and my advisor, Mike Wehr, for his support and allowing me the freedom to develop new techniques and explore surprising results. I'd also like to extend my thanks to members of the Wehr lab: Aldis Weible for teaching me implant construction and surgical techniques; Kip Keller for invaluable guidance over the years; Jonny Saunders and Ira Yavorska for their help early on and exemplifying ingenuity; Netanya Beard, Lucas Ott, and my fellow graduate students Molly Shallow, Sam Mehan, and Rocky Penick for their comradery and support; and undergraduates Tillie Morris, Thuong Le, Alexa Wright, and Olivia Estes for making the lab a great place.

I'd also like to thank my family for their encouragement during graduate school, my friends Brandon and Carrie Scholtes for all the fun times, and Lisa Wagner for being a great person. Lastly, I'd like to thank Terry Takahashi for the supportive inspiration and influence he provided me over the years.

This work was supported in part by the National Institutes of Health, National Institute on Deafness and Other Communication Disorders Grant R01 DC-015828.

TABLE OF CONTENTS

LIST OF FIGURES

Figure Page

CHAPTER II

CHAPTER III

LIST OF TABLES

CHAPTER I

INTRODUCTION

In mammals, multisensory information is combined across the neocortex and integrated into the production of behavior. How these streams of auditory, visual, and somatosensory information are converted into a common cortical framework or syntax to achieve such compatibility however, is an open question in neuroscience. In the hippocampus, theta oscillations (4-12 Hz) radiate as large-scale traveling waves, and serve as a scaffold for neuronal ensembles involved in spatial navigation, memory, and movement-related processing (Lubenov & Siapas, 2009; Patel et al., 2012; Zhang & Jacobs, 2015). An extension of such an encoding framework across the neocortex could potentially serve as a syntax in which the temporal organization of such disparate sensory signals could occur. Due to methodological shortcomings in the field of systems neuroscience however, whether similar large-scale coherent theta oscillations are present across the entire neocortex to potentially fulfill such a role is unknown.

In order to simultaneously record from large populations across the neocortex, calcium imaging in head-fixed conditions has emerged as a popular methodology in systems neuroscience. This approach is methodologically problematic for two reasons however. First, while head-fixed conditions allow the use of large and heavy equipment for physiological recordings and behavioral monitoring, it drastically alters and restricts the behavioral repertoire of the animal, and corresponding neural activity. Second, the kinetics of the protein sensors which report neural activity through the binding of calcium occur on timescales that are much slower than the electrical signaling of neurons. Results from head-fixed calcium imaging therefore often produce dynamics which do not accurately reflect the full repertoire of the animal's behavior or

corresponding neural activity.

This dissertation aims to push the field of systems neuroscience forward by addressing these two issues through the development and integration of new methodologies which allow large-scale high-fidelity cortex-wide recordings to be paired with comprehensive behavioral monitoring in freely moving mice. In Chapter II, I present a novel head-mounted camera system for monitoring freely moving mice, and demonstrate its use across an array of diverse behaviors such as prey capture, exploration, social behavior, jumping, and sleep. The significant advantages in size, weight, and cabling, allows simultaneous monitoring of the eyes, ears, whiskers, nostrils, and visual field to be integrated with large-scale electrophysiological recordings, as well as additional hardware. The flexibility of this system also allows for an incredibly wide range of configurations, enabling investigators to tailor the system to best fit their experimental goals.

Chapter II contains previously published co-authored work. It is reproduced in part and adapted from: Sattler, N.J. and Wehr, M. (2021) 'A Head-Mounted Multi-Camera System for Electrophysiology and Behavior in Freely-Moving Mice', *Frontiers in Neuroscience*, 14, p. 592417. Chapter III contains unpublished co-authored work done in collaboration with my advisor Mike Wehr.

In Chapter III, I utilize this head-mounted camera system to monitor the natural behavior of mice in freely moving conditions and discover a tight link between mouse turning and the movement of the nostrils and ears. Additionally, I develop and incorporate a method for recording bilateral electrocorticography (ECoG) in order to identify distinct cortex-wide spatiotemporal motifs of cerebral activity underlying natural behavior with sufficiently high-

fidelity. The spatial organization of cortical theta oscillations in mice has remained unknown, as the methodologies of systems neuroscience have focused on either single-cell resolution at the expense of spatial scale (i.e. local recordings from tetrodes and shanks) or spatial scale at the expense of temporal resolution (e.g. voltage or calcium imaging). Additionally, the non-invasive methodologies of electroencephalography (EEG) and functional magnetic resonance imaging (fMRI) available to the field of cognitive neuroscience have similarly forced this tradeoff of spatiotemporal resolution, while invasive methods of measuring large-scale cortical activity through ECoG are restricted to unilateral coverage in human clinical populations.

To directly investigate the spatiotemporal dynamics in high-fidelity at a cortex-wide scale, I developed a large-scale electrocorticography (ECoG) array to record across virtually the entire neocortex of freely moving mice. Theta oscillations were prominent across the cortex, and were spatiotemporally organized into three bilaterally-symmetric cortex-wide modes of oscillation which were strongly modulated by running speed. The dominant mode (Mode 1) is a bilaterally-symmetric divergent traveling wave originating in retrosplenial cortex. Modes 2 and 3 are spiral waves centered over primary somatosensory cortex. Modes 2 and 3 differed in that they exhibited opposite rotational directions, and Mode 2 displayed a high amplitude in frontal cortex, whereas Mode 3 displayed high amplitude in the temporal poles.

These traveling waves showed metastable dynamics, alternating in prominence during transient desynchronization events (known as “null spikes”) which induced a phase reset in the dominant cortical mode. Given the role of theta in the hippocampus and other cortices, these brain-wide spatiotemporal patterns of oscillatory activity may serve to integrate sensory, cognitive, and behavioral information that is distributed across the cerebral cortex. These novel findings provide

our first glimpse of cortex-wide electrocorticography, and set up the groundwork for future studies aimed at uncovering how the cortex integrates multisensory information into the production of behavior.

CHAPTER II

A HEAD-MOUNTED MULTI-CAMERA SYSTEM FOR ELECTROPHYSIOLOGY AND BEHAVIOR IN FREELY-MOVING MICE

JOURNAL STYLE INFORMATION:
Nicholas J. Sattler and Michael Wehr. Reproduced in part and adapted from *Frontiers in Neuroscience*, 2021. Supplementary videos are included as supplementary files in this dissertation.
AUTHOR CONTRIBUTIONS: NJS developed and tested the system. NJS and MW wrote the manuscript.

Introduction

Mice move. Whiskers whisk, eyes saccade, nostrils sniff, and ears pivot (Preyer, 1882; Welker, 1964; Carvell et al., 1991; Wallace et al., 2013). These active sensing behaviors have been well-established as adaptive strategies for the optimization of somatosensation (Gibson, 1962; Lederman and Klatzky, 1987; Carvell and Simons, 1995; Bagdasarian et al., 2013), vision (Ballard, 1991; O'Regan and Noë, 2001), olfaction (Mainland and Sobel, 2006), and audition (Populin and Yin, 1998; Holland and Waters, 2005; Tollin et al., 2009). Recent studies have also revealed that movement has widespread neural correlates throughout the brain. Eye movements, whisking, sniffing, running, and other classes of movements can each produce independent effects on brain regions far removed from the directly-involved motor or sensory systems (Musall et al., 2019; Stringer et al., 2019; Salkoff et al., 2020). Investigating sensory processing therefore requires either that all movements are eliminated (e.g., by head or eye fixation), or that they are accurately measured. Despite the insights that have been gained from research under head-fixed or eye-fixed conditions, there has been a growing appreciation that understanding brain function will require recording neural activity in freely-moving animals, especially during ethological behaviors (Datta et al., 2019; Parker et al., 2020). Yet monitoring the simultaneous movements of the eyes,

whiskers, nose, ears, limbs, and the rest of the body in freely-moving conditions and with high-density electrophysiology remains methodologically challenging.

There are many inherent technical difficulties when designing attached devices for freely-moving behaviors in small animals. Every component comes with an associated cost of size, weight, positioning, balance, and cabling. Each of these factors necessarily constrains the free movement of the animal, and the magnitude of their effects scale inversely with the animal's size and strength. The first rodent head-mounted camera system was developed to monitor the behavior of freely-moving rats, with each attached camera weighing 800 mg (Wallace et al., 2013). A more recent breakthrough was the development of a head-mounted system for monitoring both behavior and electrophysiology in mice, with each attached camera weighing 500 mg (Meyer et al., 2018). Mice are an order of magnitude smaller than rats however, therefore requiring significantly smaller and lighter head-mounted devices. Here we describe a promising new system for monitoring physiology and behavior in freely moving mice, with significant advantages in size, weight, cabling, signal quality, and customizability. The key advance is the use of miniature analog camera modules (180 mg, 5 × 5 × 5 mm), allowing for lightweight multi-camera headsets, finely-focused video signals, and single-ended signal connections for low-impact tethering.

We present two examples of multi-camera headsets for use with electrophysiology: a headstage-integrated four-camera headset, and an adjustable two-camera headset. We then provide further examples of their implementation, and discuss general guidelines for designing a specific implementation of this system to best suit your experimental goals.

Results

Four-Camera Headset

First, we describe a four-camera headset, designed as an attachment for the Intan 32-channel electrophysiology headstage. The four cameras provide an independent view of each of the two ears, an overhead view of the eyes, whiskers, and rhinarium, and a forward-facing view of the visual scene. Figure 1 and Supplementary Video 1 show an example of the signals from this four-camera headset as a mouse explores an object in an open-field arena. Pupil diameter, gaze direction, whisking, and rhinarial movements can be measured from the overhead camera, and ear movements can be measured from the ear-facing cameras.

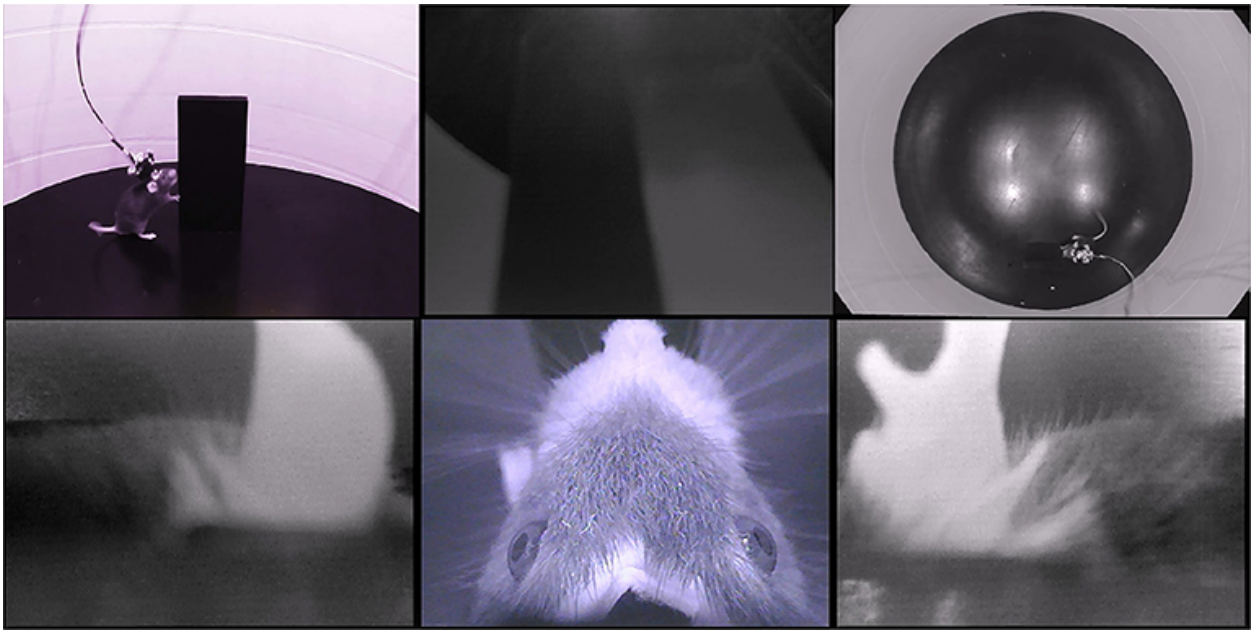

Figure 1. Example data from the four-camera headset.
An example frame from Supplementary Video 1, showing the webcam views of a mouse exploring an open arena, from the side (top left) and above (top right), and the video signals from the four-camera headstage-integrated headset: left ear camera (bottom left), right ear camera (bottom right), overhead camera (bottom middle), and forward-facing camera (top middle). Note that the overhead camera video signal is of higher quality than the front-facing or ear-facing videos, due to their filtering.

The four-camera headset weighs a total of 1.64 g (Table 1). When combined with an electrophysiology headstage, and an implanted tetrode microdrive, electrode interface board (EIB), and an implant base (Figure 2Ai), the total weight of the system is 3.51 g. Camera headsets consisted of analog camera modules assembled on a 3D-printed camera carrier (Figure 2Aiii), which attaches to the Intan headstage (Figures 2B,C). Integrating cameras with the headstage in this way allows electrophysiology, accelerometer, and video signals to be collected with a single mechanical attachment to the head (at the EIB), which simplifies experimental setup and reduces the overall weight. This design also allows for stereotactic precision and reproducibility of camera views across animals and implants by combining the fixed dimensions of the implant with the stereotactic targeting of the electrodes. Additionally, the focal plane of each camera can be easily adjusted to accommodate for surgical or anatomical jitter encountered between animals (see section "Reproducibility and Precision" below for more details). When the factory-installed lens on the camera modules is maximally extended, the field of view is ~12 × 9 mm at the level of the focal plane, which is ~12 mm away. By screwing the lens all the way in, the camera's focal length increases toward infinity, with a corresponding increase in field of view.

Each camera requires three electrical connections: a power, ground, and signal. With this headset design, the four cameras share power and ground connections, thereby only requiring a six-conductor tether (or six individual wires). The common ground introduces interference in the video signals caused by high-frequency crosstalk, but this interference can be removed through the use of simple low-pass filters (see section "Powering and Signal Conditioning" below for more details). One camera can remain unfiltered, yielding a higher quality video signal. We chose the overhead camera in this case, to achieve finer detail of the eyes, whiskers, and rhinarium.

Number of cameras	1	2	4	8
RS-306 camera alone (g)	0.18	0.36	0.72	1.44
RS-306 camera assembly (g)	—	0.68	1.64	2.16
RS-306 Electrophysiology/camera assembly (g)	—	2.56	3.51	4.03
Adafruit 1937 camera alone (g)	0.5	1.0	2.0	4.0
Adafruit camera assembly (g)	1.28	2.55	5.10	10.24
Adafruit Electrophysiology/camera assembly (g)	4.28	5.55	8.10	13.24

Table 1. Weight comparisons.
Camera assemblies include the cameras, structural carrier, LEDs, resistors, wiring, and connectors. Adafruit assembly also includes IR mirrors. Our 2-camera and 4-camera assemblies correspond to the configurations used in Figures 4C, 2A, respectively. We have not constructed an 8-camera headset but rather estimated weights from the parts shown in Figure 6. "—" indicates not tested, since we only constructed multi-camera headsets. Electrophysiology/camera assembly includes a camera assembly, electrophysiology headstage (Part #17), EIB (Part #32), and implant base (Part #27). Weights for the Adafruit camera assembly are from the single-camera system described in Meyer et al. (2018), which we extrapolated for multiple cameras. The weight of the Adafruit/Electrophysiology/camera assembly was estimated by adding an electrophysiology headstage (Part #17, 1 g) and flexDrive (Voigts et al., 2013, 2 g), but does not include the weight of a custom aluminum implant base (Meyer et al., 2018). Mass of cement and/or skull screws is not included. An adult mouse can support ~4 g at most (Voigts et al., 2013).

This headset design has some drawbacks compared to the two-camera headset described below. Once assembled, the camera positioning is not adjustable, requiring iterations of building, and testing to optimize camera angles for each use-case. Additionally, while this headset arrangement allows for a large view of multimodal behavior, the overhead perspective may miss a portion of the pupil in rare cases of extreme ventral gaze. Lastly, because the headset is fully integrated, if one component were to fail, it may be difficult to individually replace it without rebuilding the entire headset (although the camera modules can be reused).

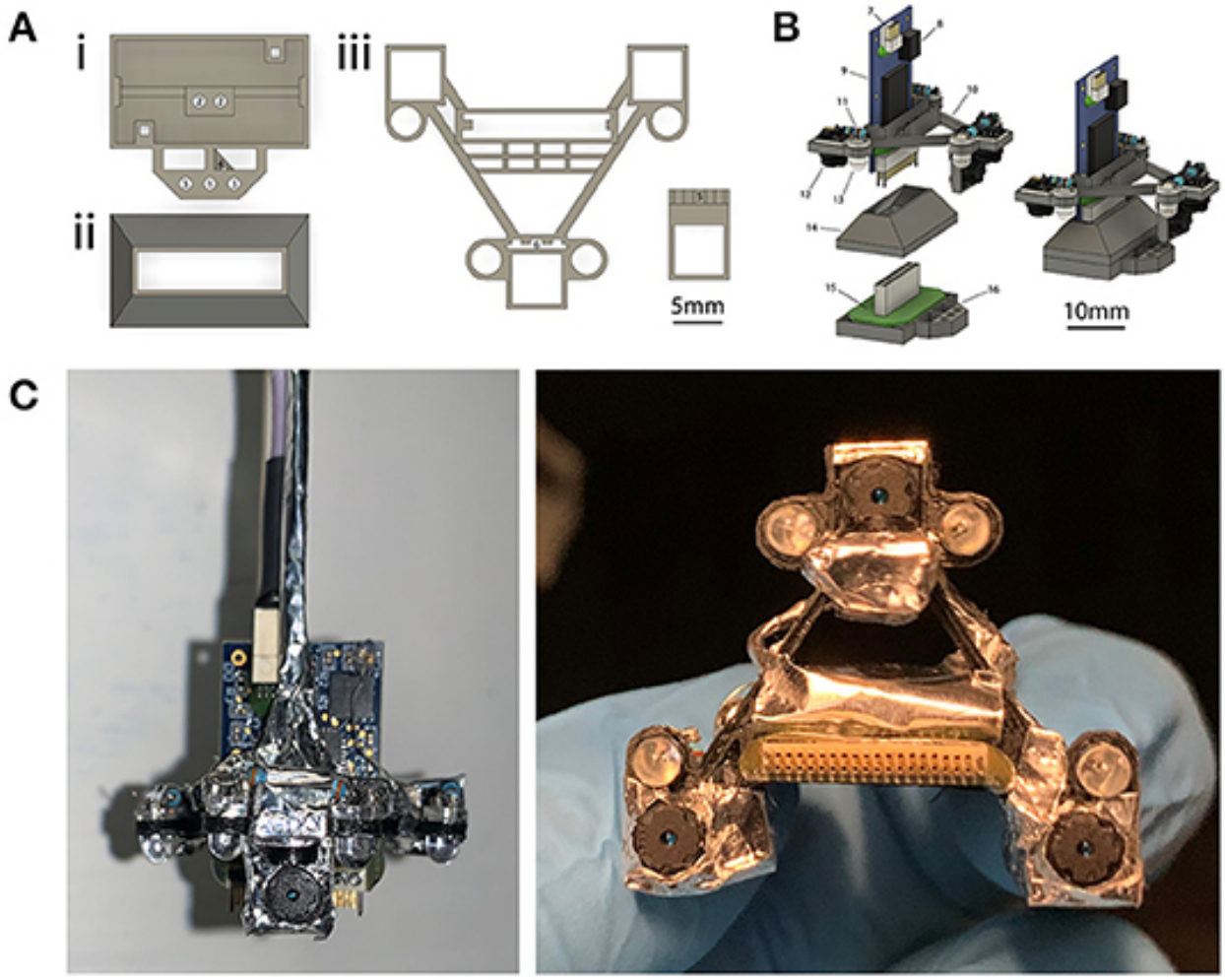

Figure 2. Four-camera headset design.
(A) 3D-printed components used for implants and headsets. (i) Implant base that is implanted on the head. A Neuralynx EIB is attached to the implant base. (ii) Protective cap that snaps onto the implant to allow for social housing when the camera assembly is not in use. (iii) Camera carrier that holds the cameras and their associated LEDs. The ear-facing cameras are each paired with a single LED for illumination, whereas the overhead camera has two LEDs (for illuminating the left and right side of the mouse's face), and the forward-facing camera does not have an LED. The forward facing camera holder is attached to the main camera carrier component after printing. Numbered labels indicate (1) tetrode drive screw, (2) tetrode guide rails, (3) optional independent camera mount, (4) tetrode guide cannulae, (5) forward camera holder (6) receiving slot for forward camera holder. For further details on labels 1–4 see section Methods: Implants, for labels 5–6 see section Methods: Four-Camera Headset, Construction. **(B)** Rendered view of the components in **(A)**, separately at left and assembled at right. Numbered labels indicate (7) SPI cable connector, (8) integrated accelerometer, (9) Intan 32-channel headstage, (10) camera carrier, (11) resistor, (12) camera module, (13) IR LED, (14) protective social cap, (15) Neuralynx EIB, and (16) implant base. **(C)** A view of the headset assembled around the headstage from the front (left) and underneath (right).

Adjustable Two-Camera Headset

Next, we describe an adjustable two-camera headset as shown in Figure 3A, designed to consistently view the entirety of both pupils, and to capture all eye movements in higher detail. To provide the highest-quality video signal, both cameras have independent signal, power, and ground connections for full signal integrity (see section "Powering and Signal Conditioning" for more details).

While this headset is not necessarily integrated with an electrophysiology headstage, it can be easily paired with one. Example waveforms and rasters of unit activity recorded in anterior lateral motor cortex (ALM) during prey capture behavior are shown in Figure 3B and Supplementary Video 2. Single neuron recordings were stable across many days. Raw continuous traces of local field potentials (LFPs) recorded from several different brain areas during courtship behavior are also shown in Figure 3C and Supplementary Video 3 (see sections "Implants," "Surgery," and "Experimental Conditions" for more details).

Figure 3. (next page) Two-camera headset, and two example applications of freely-moving behavior and electrophysiology.
(A) Rendered view of the two-camera headset (left), and an example frame from Supplementary Video 2 showing the signals produced by this headset (right). A collimating lens (revealed on the right side of the render) was used for some experiments, but is not necessary for capturing all eye movements. **(B)** Example waveforms across the four channels of a tetrode shown for an individual unit (cell ID 1) recorded in anterior lateral motor cortex (ALM) during prey capture behavior. Rasters of cells firing and the accelerometer channels are plotted together (right) for the corresponding frames shown in **(A)**. The accelerometers are built into the Intan headstage. **(C)** An example frame from Supplementary Video 3. The left eye is closed (due to a blink). A spectrogram (top) shows ultrasonic vocalizations occurring during courtship behavior. Continuous LFP traces from various recording locations are shown below. OLF, olfactory bulb; ALM, anterior lateral motor cortex; ACC, anterior cingulate cortex; Hip, CA1 of the hippocampus; S1BF, barrel field of primary somatosensory cortex; S2, secondary somatosensory cortex; A1, primary auditory cortex; A2, secondary auditory cortex.

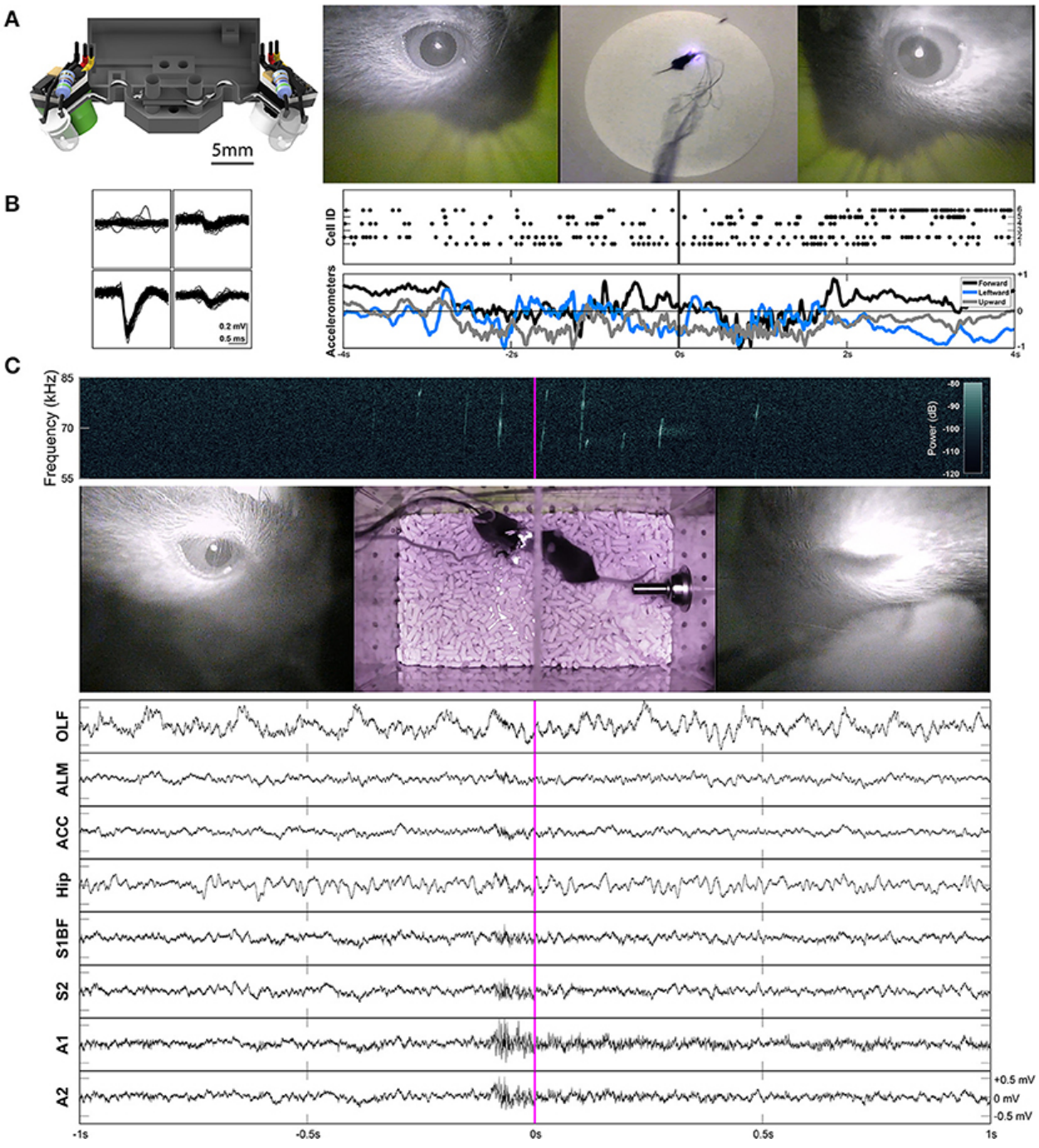
A
5mm
B
0.2 mV
0.5 ms
Cell ID
Accelerometers
Forward
Leftward
Upward
-4s
-2s
0s
2s
4s
C
Frequency (kHz)
85
70
55
Power (dB)
-80
-90
-100
-110
-120
OLF
ALM
ACC
Hip
S1BF
S2
A1
A2
+0.5 mV
0 mV
-0.5 mV
-1s
-0.5s
0s
0.5s
1s

With the camera module's factory-installed lens fully extended and focused on the surface of the iris, these cameras can detect cyclotorsion of the mouse eye. Examples of this behavior can be seen in Figure 4 and Supplementary Video 4, which show torsional rotations of up to 11° in extent, at rotational rates of up to 4.6°/s. During periods of active movement, these rotational events occurred frequently, on average at 0.3 events per second in this example mouse.

We tracked cyclotorsion using the unique pattern of natural serrations of the mouse eye in a manner similar to iris-registration software used to track torsional movements in humans during laser eye surgery (Shen et al., 2010). These serrations appear above the lens, at the pupillary rim of the iris, and vary between individual mice. Tracking these serrations allows torsional position to be determined without the use of more invasive techniques, such as limbal markings (Shen et al., 2010), scleral search coils (Robinson, 1963), or other magnetic implants (Schwarz et al., 2013). Our initial design used a collimating lens as shown in Figures 3A, 4A, which was subsequently adopted by others (Michaiel, 2019; Michaiel et al., 2020). We have since found that this lens is unnecessary for capturing all eye movements, and is not included in the final design (Figure 4B).

Figure 4. (next page) Headset components pictured with their total weight (left) and examples of their video signals (right).
(A) A camera headset consisting of two camera modules, resistors, external IR LEDs, and collimating lenses (left), and an example frame from Supplementary Video 4, showing the right eye (middle). The inset marks the cropped location of the enlarged images of the pupil (right) from four consecutive deinterlaced frames of Supplementary Video 4 at 60 Hz, with optic flow vector fields between successive frames shown underneath. Dashed red lines mark the orientation of prominent serrations across the pupillary rim of the iris in the first frame. Solid red lines track these serrations in consecutive frames. See Supplementary Video 4 for the full video. Optic flow was calculated in Matlab using the Lucas-Kanade derivative of Gaussian method with a noise threshold of 0.0005, and plotted with a scale factor of 100. **(B)** A camera headset consisting of two camera modules, resistors and external IR LEDs (left), and example frames of the video signals produced under white houselights, no houselights (darkness), and infrared houselights (right). See Supplementary Video 4 for example footage under white houselights. **(C)** A camera headset

consisting of two camera modules, one resistor, and one IR LED chronically implanted above a cranial window for infrared back-illumination pupillometry (iBip), and example frames of the video signals produced under white houselights, no houselights (darkness), and infrared houselights (top right). See Supplementary Video 4 for example footage under white houselights, and Supplementary Video 5 for example footage in darkness, displaying the fundus, and optic disc. Example frames of wake, NREM sleep, and REM sleep recorded in the nest of the home cage (bottom). See Supplementary Video 6 for the full video.

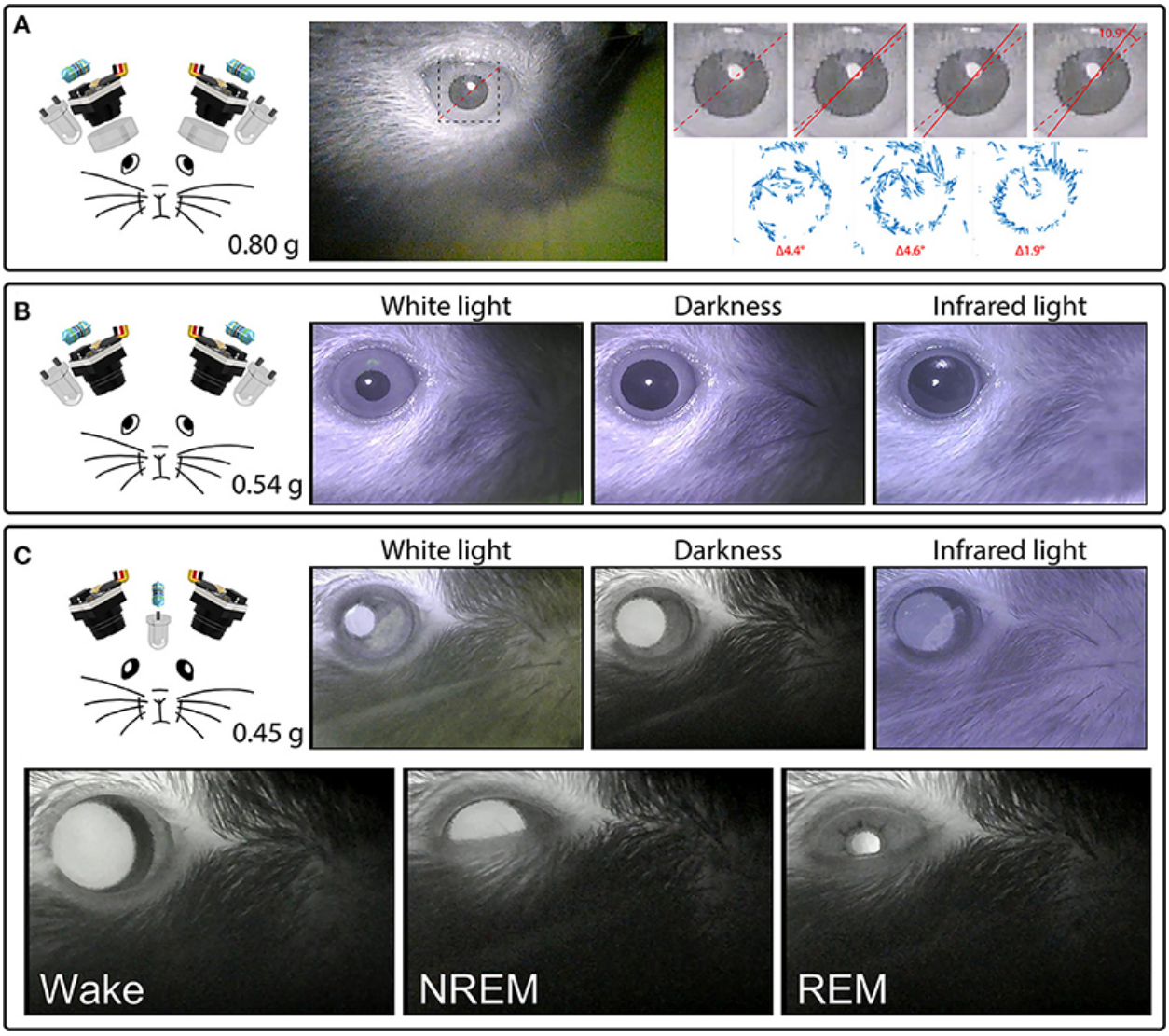

While epi-illumination of the eyes with external IR LEDs provides a consistent video signal across lighting conditions as shown in Figure 4B, infrared back-illumination pupillometry [infrared back-illuminated pupillometry (iBip); (Yüzgeç et al., 2018)] is an alternative approach that can be used with our system. In this configuration, an IR LED is implanted over the skull and back-illuminates the pupil from inside the head. This allows the monitoring of the pupil and torsional position using fewer LEDs and resistors, as shown in Figure 4C and Supplementary Video 4 (see sections "Implants" and "Surgery," for more details). This method of illumination reveals structures that are not otherwise visible through epi-illumination: prominent natural markings of the iris as shown in Supplementary Video 4, which can provide large and obvious markers for tracking torsional position, and the fundus, retinal vasculature, and optic disc as shown in Supplementary Video 5, which provide the necessary anatomical landmarks to translate the absolute position of the iris into true retinal coordinates. Additionally, utilizing iBip with this system is well-suited for providing robust pupillometric monitoring across both wake and sleep in natural freely-moving conditions. Figure 4C and Supplementary Video 6 show examples of wake, NREM sleep, and REM sleep—characterized by their behavioral hallmarks—from an unrestrained mouse in the nest of the homecage (Yüzgeç et al., 2018; Blumberg et al., 2020).

Lastly, the mounting system of this headset uses steel wire and cement, rather than a 3D-printed carrier, which allows the camera angles and positioning to be adjusted by bending the steel wires. Supplementary Video 7 shows an example of an alternative camera perspective generated by simply bending the wires (for a more dorsal view of the eye and whiskers), illustrating how this mounting system is useful for testing different camera angles in pilot experiments (in this case, as a mouse performs a jump). While this mounting strategy of bending wires lacks exact reproducibility

across headsets, reproducibility of camera views across animals and implants can still be achieved for an individual headset by combining the fixed dimensions of the implant with the stereotactic targeting of the electrodes and *post-hoc* calibration of their geometric positioning. Ultimately, once the spatial arrangements of the components have been optimized for your desired signal(s), the headset could be adapted to use a 3D printed carrier, similar to the four-camera headset described above. Even during rapid behaviors such as jumping, we did not observe any motion artifacts in recorded video (e.g., Supplementary Video 7), although the steel wire headset is susceptible to minor motion artifacts in the case of a high-speed collision with a wall (as in Supplementary Video 2). We did not observe motion artifacts with 3D-printed carriers, nor did the camera headsets introduce any motion artifacts into electrophysiology signals.

For either headset configuration, the headstage can provide power and ground connections of the correct voltage for the cameras, reducing the tether requirements even further, but at the cost of introducing appreciable levels of 60 Hz noise into the electrophysiology channels. The level of noise with headstage-provided power is unacceptable for LFP recordings, and for small-amplitude single neuron recordings, but could allow isolation of large-amplitude single neurons. We therefore recommend powering the cameras through the tether from an external source to ensure high-quality and noise-free electrophysiology.

Discussion

All animals move. Whether these are active sensing behaviors such as saccades or whisking, or large-scale movements directed at broader goals such as capturing prey or returning home, the effects on sensory input are profound. Movement also has a substantial impact on brain activity even beyond the directly-involved sensory and motor areas (Musall et al., 2018;

Stringer et al., 2019; Salkoff et al., 2020). To understand how the brain underlies both sensation and action during freely-moving behavior, whether natural behavior or choice tasks, will therefore require precise measurement of the movements of the eyes, ears, whiskers, and rhinarium.

Here we have presented a head-mounted multi-camera system for the simultaneous recording of multiple body parts, sensory structures, and the visual scene, along with high-density electrophysiology in freely-moving mice. The core components are lightweight (180 mg) and inexpensive (US$23) analog camera modules with a number of advantages that increase the flexibility of implementation compared to previously published alternatives. Their size, weight, and cabling advantages allow multi-camera headsets to monitor more sensory structures and capture more of the visual field, while their low impact on behavior enables chronic monitoring under natural conditions across the sleep-wake cycle. Additionally, the system can provide high-precision tracking of eye movements, such as cyclotorsion, and allows the absolute position of the eyes to be translated into true retinal coordinates via visualization of the fundus and optic disc. Together, these features allow the alignment of neuronal activity with both motor events and retinotopically mapped visual stimuli in freely-moving animals.

Although we provide examples of specific configurations for monitoring certain body parts and views (i.e., the eyes, ears, whiskers, and binocular visual field etc.), we anticipate that this system will be adapted to best suit specific experimental goals using the strategies and considerations presented below.

Size, Weight, and Multi-Camera Headsets

Size and weight are perhaps the most crucial aspects of head-mounted devices, and together are significant advantages of this system compared to previously published alternatives. Because analog camera modules forgo on-chip digitization of the video signal, ADC hardware components are eliminated from the design at the level of the animal, resulting in a significant reduction of both size and weight. At 5 × 5 × 5 mm and 180 mg, the size and weight of these camera modules serve to minimize their effects on mouse behavior. Figure 5 shows the differences in size and weight between these camera modules (the LeeChatWin RS-306) and the Adafruit 1937 camera, a leading alternative for behavioral monitoring of freely-moving mice (Meyer et al., 2018).

The primary benefit of this is to reduce the load carried by the animal, which in turn leads to a number of corollary benefits. First, cameras can be much more readily incorporated with larger and heavier hardware, such as electrophysiology headstages, and positioned in much closer quarters due to their size and flexible cabling options. Second, more cameras can be used to monitor additional body parts and classes of movements. Using more cameras is likely to be important, as recently described brainwide correlates of high-dimensional motor variables show the importance of capturing as much behavioral information as possible (Musall et al., 2019; Stringer et al., 2019). Third, more cameras can be used to capture more of the visual field, and at the same time can be packed closer together to obstruct less of the visual field. Fourth, mirrors are not required to achieve desired viewing angles, because the cameras themselves are light enough to extend distally from the head. This greatly reduces the complexity of headset designs as well as reducing overall weight. All together, these advantages allow the construction of multi-camera headsets to be much more feasible, as illustrated in Figure 6 which shows an example rendering of

an 8-camera headset designed to capture the entirety of the binocular visual field while also monitoring both eyes.

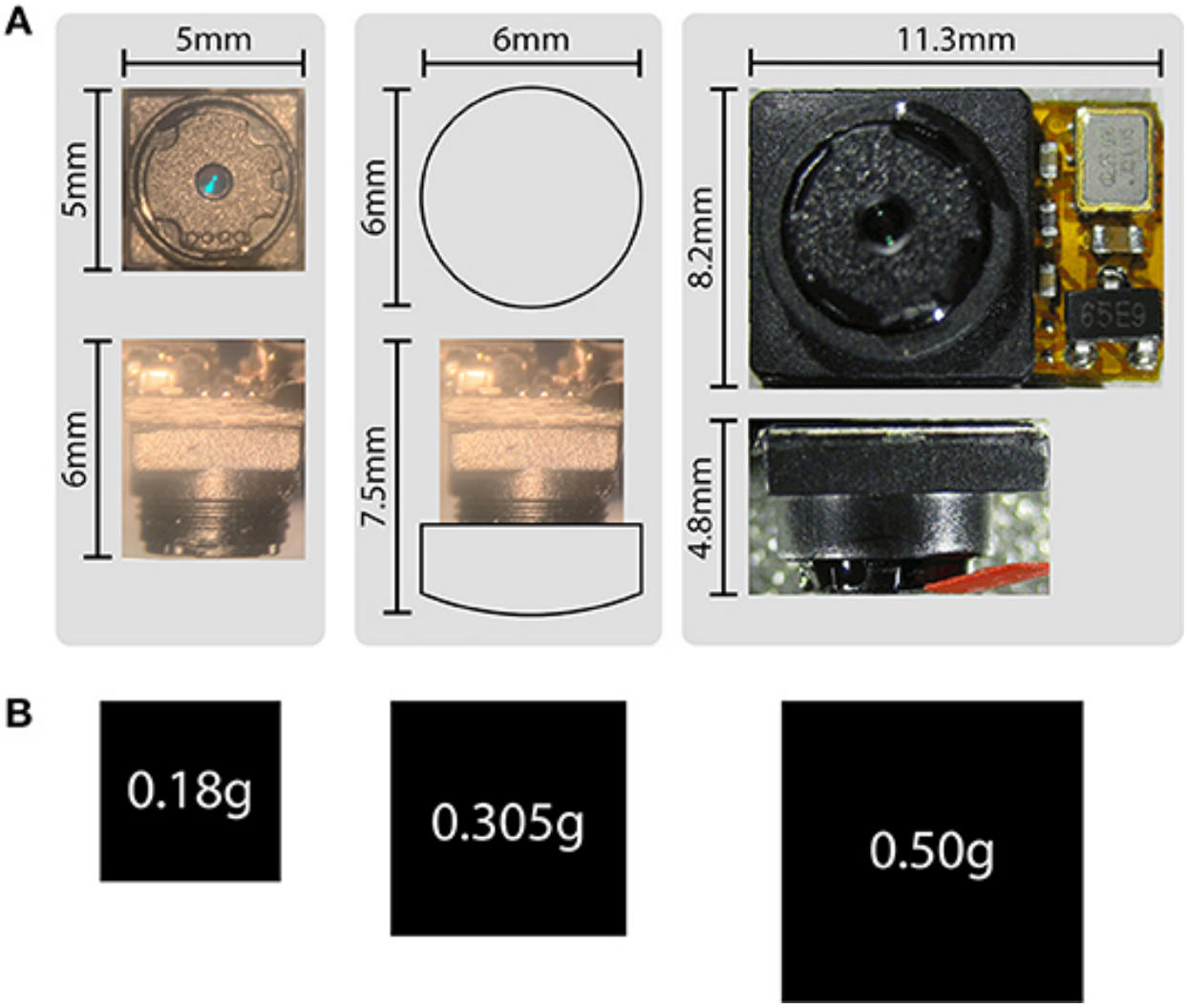

Figure 5. Size and weight comparisons.
(A) Size comparisons between the analog camera modules (left), analog camera modules with an additional collimating lens (middle), and an Adafruit 1937 picam camera module (right). The factory-installed adjustable lens has 1 mm of travel, and is shown maximally extended (left, for a total camera depth of 6 mm), and minimally extended (middle, for a camera depth of 5 mm, or 7.5 mm with the additional collimating lens). Broader views of the camera modules are also shown in Appendices 1, 2 (see APPENDICES FOR CHAPTER II for all appendices). **(B)** Weight comparisons represented by area for the corresponding camera modules shown in **(A)**.

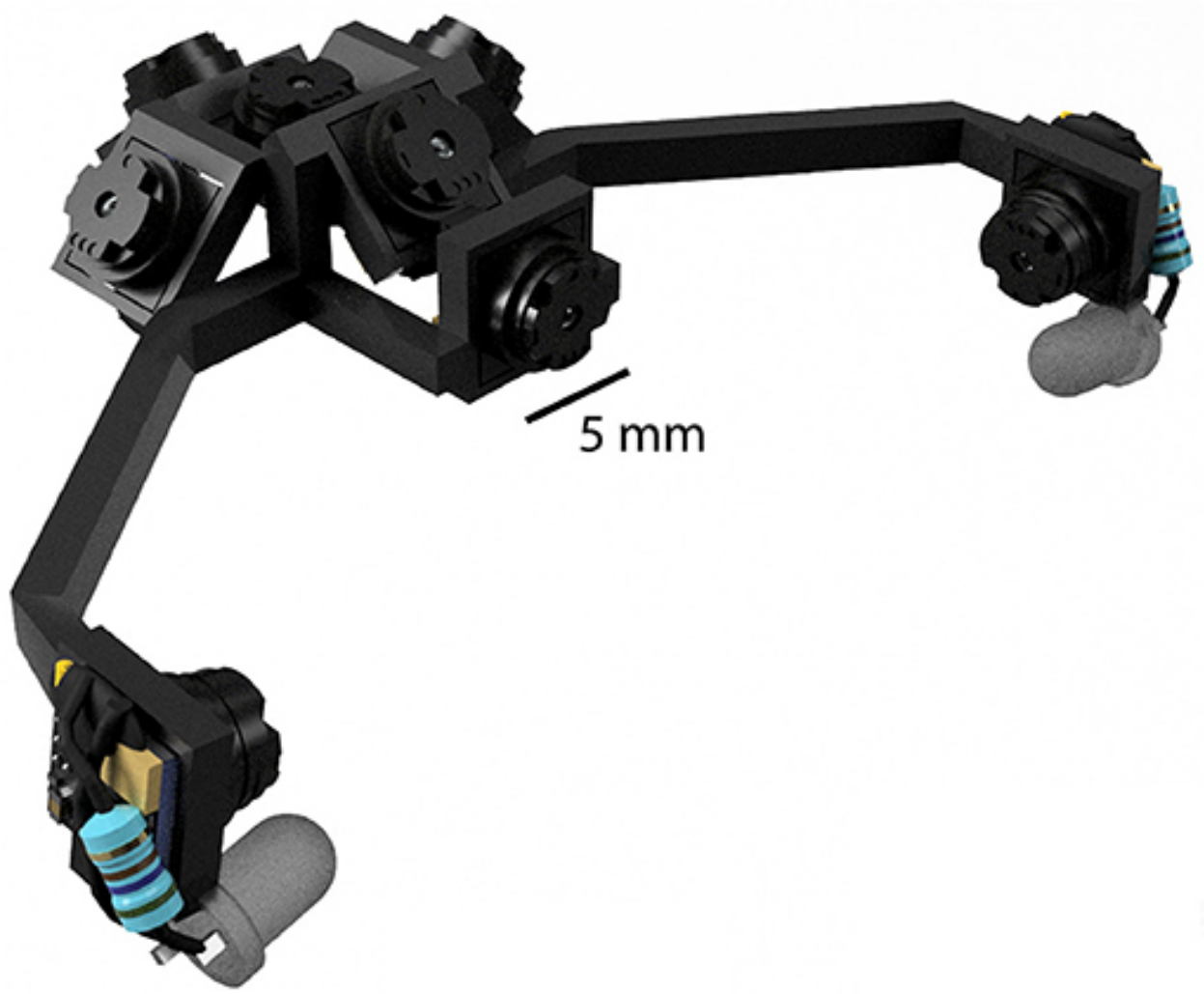

Figure 6. An example rendering of an 8-camera headset designed to capture the binocular visual field while monitoring the eyes. Although a mouse could additionally support the weight of an electrophysiology headstage and EIB, the headstage would necessarily occlude some portion of the visual field.

How many cameras could a mouse support? There is no fixed maximum load for head-mounted devices, because capacity depends on the size and strength of each individual. Moreover, the impact to mouse behavior increases smoothly with load rather than suddenly reaching a threshold, and the negative consequences will depend on the behavioral task in each experiment. Nevertheless, it is straightforward to compare the maximal number of cameras across systems for a

given load limit. For example, a load limit of 4 g would permit 8 cameras and a 32-channel electrophysiology headstage (Table 1), whereas with the Adafruit 1937 only 1 camera and a headstage would be possible (Meyer et al., 2018).

The four-camera electrophysiology headset described above, including the electrophysiology headstage, weighs a total of 3.5 g, for minimal effects on natural behaviors such as prey capture and vocal interaction. While the RS-306 camera is significantly smaller and lighter, the Adafruit 1937 camera has superior temporal resolution, capable of capturing digital 640 × 480p frames at 90 Hz. The Adafruit 1937 can also be configured to capture 1,080p frames at 30 Hz, or 720p frames at 60 Hz. Taken together, the size and weight advantages of our system are significant, but the lower temporal resolution of the analog cameras (60 Hz compared to 90 Hz with the Adafruit 1937) presents a trade-off that depends on individual experimental requirements.

Cyclotorsion

Natural cyclotorsion of the eye has been observed in pigeons (Benjamins and Huizinga, 1929), chickens (Schwarz et al., 2013), rats (Preyer, 1882; Welker, 1964; Carvell et al., 1991; Wallace et al., 2013), and primates (Wells, 1794; Helmholtz, 1925), but to our knowledge has not previously been described in mice. Cyclotorsion is known to interact with the vestibular system to provide gaze stabilization as the head rotates about an axis of fixation or an object of smooth pursuit (Tweed and Vilis, 1987; Crawford et al., 1991; Angelaki and Dickman, 2003). The occurrence of cyclotorsion events up to 11° in mice highlights the importance of capturing all eye movements for studies of vision in freely moving animals (Ballard, 1991), and its necessity for studies that seek to relate retinotopic receptive fields to visual stimuli or behavior (Cooper and Pettigrew, 1979).

Absolute Retinal Position and Retinotopic Mapping of Visuotopic Space

The absolute position of the iris corresponds to the absolute position of the retina (Felius et al., 2009). However, the features of the iris are unique between individuals and lack any predefined location around the pupillary rim. Translating the torsional orientation of the iris into the torsional orientation of the retina therefore requires a geometric calibration between at least two points on both the iris and the retina to establish their alignment. This requires anatomical landmarks on the mouse retina to establish its torsional orientation in reference to the camera's position. With the lack of a visible macula in mice (Volland et al., 2015), the optic disc and retinal vasculature may be the only readily visible anatomical landmarks on the retina with which torsional position can be established (Parsa and Kumar, 2013). Using our system with iBip reveals the optic disc and retinal vasculature, and allows them to be visualized together with the features of the iris (Supplementary Video 5). This provides the necessary anatomical landmarks from the common perspective of the camera, such that the torsional position of the iris can be used to determine the torsional position of the retina. Calibration of anatomical retinal coordinates to absolute visuotopic coordinates requires an additional step to anatomically identify the visual midline (as described in detail by Sterratt et al., 2013). With the use of modern inertial measurement devices and video tracking to determine the camera's absolute position and orientation, this calibration can then be used with the absolute position of the pupil to project retinotopic coordinates onto visuotopic space (Sterratt et al., 2013; Wallace et al., 2013; Matthis et al., 2018). Utilizing iBip with this system is therefore particularly well-suited for experiments seeking to link neuronal activity in retinotopically organized brain areas with visual stimuli in freely moving conditions.

Tethers

For head-mounted video, tethers will likely remain necessary until further advances in power and high-bandwidth telemetry or local data storage become available. As a mouse turns, tethers accumulate torque which strains their free movement and may bias their decisions. Importantly, since this system uses individual wires for signal and power connections, there are many available options of fine flexible wire to choose from as opposed to the flat ribbon cables of the Adafruit 1937 camera. Additionally, they can be readily integrated into slip ring commutators and pulleys to relieve strain from the tethers, which may prove more difficult with a ribbon cable. Using modern commutators which utilize close-loop systems to provide active accommodation could also be implemented to relieve any strain of the electrophysiology and camera tethers, as well as optical fibers (Hoshino et al., 2020). Active counterbalancing of the tethers through closed-loop tracking and motorized pulleys should also be possible, however we have not yet tested motorized commutators or pulleys with this system. Lastly, these tethers can directly power LEDs, which allows them to be easily integrated into headsets without requiring additional tethers or electrical connections to additional implanted hardware.

Reproducibility and Precision

The precise positioning of electrodes and cameras is limited by the surgical jitter of implants and individual anatomical differences across mice. The solution we described here is to integrate conventional stereotactic targeting with 3D-printed implant design. A promising framework for these types of implants is the RatHat, which is an open-source self-targeting 3D-printed brain implant system (Allen et al., 2020). Manual adjustment of the fine focus of the individual camera modules can also help compensate for remaining differences in focus

encountered between animals. Taking note of the markings on the face of the lens when adjusting between animals is helpful for reproducibility in this case.

General Design Guidelines

Other undesirable consequences of all head-mounted devices include partial occlusion of the visual field, interference with sound localization due to sound shadows, and interference with access to apparatus components such as nosepokes. For these reasons, camera headsets should be designed with specific experiments in mind, to balance the benefits of the desired behavioral and physiological signals with their impact on sensation and behavior.

When customizing the camera set-up to target different camera views, electrode locations, or other hardware, we recommend the following design considerations. First, determine the locations of optical fibers or microinjection ports, which require open access during experiments. The EIB should then be placed where it doesn't impede this access. A different choice of EIB or the use of silicone probes will likely affect this placement. The implant base should then be designed and positioned to accommodate the EIB and other hardware. Finally, design the camera carrier based on how it will mount to the implant base or EIB, in order to target the cameras at the desired viewpoints.

Future Directions

We envision a number of extensions for this system. Firstly, utilizing open-source frameworks for 3D-printed stereotaxic implants, such as the RatHat (Allen et al., 2020), will allow the targeting of electrodes, cameras, optical fibers, and other components to be unified within and across animals, implants, experiments, and labs. The use of high-density silicon probes, such as neuropixel arrays (Steinmetz et al., 2020), will dramatically increase the number

of neurons that can be recorded alongside head-mounted video, and a common framework for 3D stereotaxic implants will therefore enable more replicable designs, experiments, and analyses, as hardware components continue to evolve and improve.

Integrating such a framework into open-source libraries for experimental design, such as Autopilot (Saunders and Wehr, 2019), will also allow for increased ease of use and replicability of experimental setups and analysis. These efforts to standardize data organization may also serve to streamline experiments which require several processes of analysis and reconstruction techniques using various software packages, such as Kilosort (Pachitariu et al., 2016), DeepLabCut (Mathis et al., 2018), or Retistruct (Sterratt et al., 2013).

Finally, we have not explored the upper limits on the number of camera modules that can fit on the head and be supported by a mouse without noticeably impacting behavior. Improvements in implant design and tether choice will improve efficiency and will likely continue to increase the number of devices that can be included. Optical imaging of neural activity using these sensors may also be a promising approach. A widefield miniscope using this analog camera module could be integrated with behavioral camera arrays, like those in Figure 1 for example, to investigate large-scale brain activity in freely moving conditions.

Methods

Preparation of Camera Modules

We used LeeChatWin RS-306 miniature analog camera modules (Part #1), but other miniature analog camera modules with similar specifications are available from a range of manufacturers. Before modifying the cameras in any way, we ensured that they produced a clean and stable video signal out of the box by powering the camera's attached barrel cable with a 12V

DC power supply and connecting its RCA composite video connector to a display. We then removed the infrared filter as described in Appendix 1 (see APPENDIX FOR CHAPTER II for all appendices), cleared away excess rubber as described in Appendix 2, and stripped insulation from the leads as described in Appendix 3.

Four-Camera Adjustable-Focus Headset

Construction

All 3D-printed components (Figure 2A) were designed and rendered with Autodesk Fusion 360 software (Part #2), prepared using Cura (Part #3), and printed with polylactic acid (PLA) on a Monoprice Maker Select Plus 3D Printer (Part #4).

We 3D-printed a camera carrier (Part #5) as shown in Figure 2Aiii. The carrier was inspected and tested to ensure the camera modules would properly fit into each camera holder as described in Appendix 7. We then applied a thin coat of superglue to the grooves of the forward camera holder (marked 5 in Figure 2Aiii), and inserted it into the corresponding slot in the camera carrier (marked 6 in Figure 2Aiii, also see photo in Appendix 7).

To create the headset, we first prepared a wiring harness with measured segments of wire needed to power the IR LEDs and camera modules on the headset (Appendix 4). We then soldered the prepared wires to each camera module (Appendix 5), shielded them with aluminum tape (Appendix 6), and cemented them onto the headset (Appendix 7). We then inserted the IR LEDs into the receiver holes in the carrier and soldered the leads to their respective camera module (Appendix 8). The IR LEDs provide constant and sufficient illumination of the eyes, ears, or face during experiments regardless of head position, while this illumination remains invisible to the mice. Next, we soldered the power wires to a single power tether, and the ground wires to a single

ground tether (Appendix 9). We then applied the last piece of shielding (Appendix 10) and attached the headset to an Intan headstage by inserting the headstage into the receiver slot in the carrier, and then sliding the carrier all the way down onto the headstage (Appendix 11). A friction fit is sufficient to keep the headset firmly mounted to the headstage indefinitely. Repeated attaching and detaching of the headset to headstages could cause wear and tear and is not recommended. Finally, we electrically connected all the shields and pinned them to the local ground of the headstage (Appendix 12).

Powering and Signal Conditioning

We terminated the ends of the signal, power, and ground tethers with male jumpers for easy connection/disconnection. We used a +3.3V terminal on an RHD2000 USB interface board to power the cameras for use with or without accompanying electrophysiology, but any +3.3V power supply should work. The cameras could optionally be powered directly by the headstage as well, reducing the number of wires in the tether and still allowing accelerometer signals to be acquired, but at the cost of introducing noise on the electrophysiology channels.

The 4 cameras can share power and ground connections, thereby using only 6 wires, but the common ground introduces interference caused by high-frequency crosstalk (producing chrominance and dot-crawl noise). If additional wiring is not a consideration, this interference can be avoided by using independent power and ground connections for each camera (i.e., 12 wires for 4 cameras). Alternatively, the interference can be removed with simple low-pass filters (we used a 560 Ω resistor in series with each video signal). We constructed these filters on a separate breadboard for the camera signals, and integrated it into the system as shown in Figure 7. One camera signal can remain unfiltered, yielding a higher quality video signal.

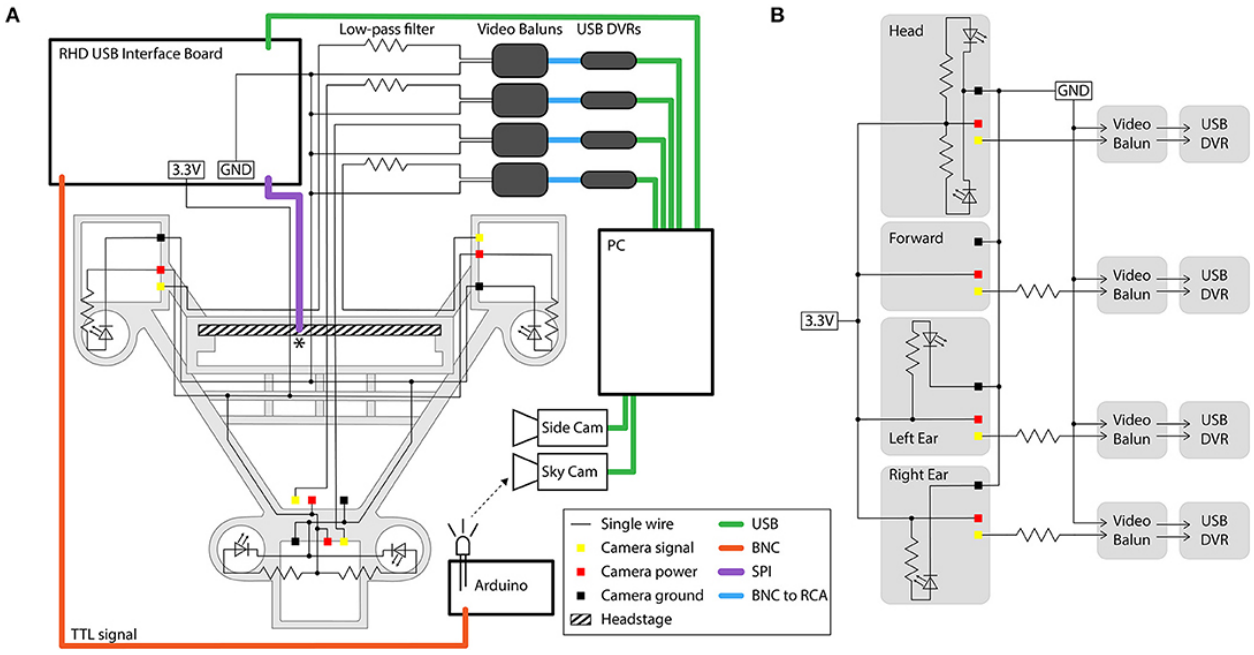

Figure 7. Circuit diagram and connections for the four-camera headstage-integrated headset. **(A)** The camera carrier (same as Figure 2Aiii) is shown in the background in gray. The RHD 32-channel headstage is represented by the hatched rectangle, and is attached to its associated SPI cable represented by the purple line at the point marked *. TTL pulses sent to the RHD 2000 USB Interface Board are relayed through a BNC cable (orange) to an Arduino Uno for synchronization of electrophysiology and video signals by illumination of an IR LED in view of the webcam placed above the arena (the SkyCam). Yellow, red, and black squares represent the soldering locations on the camera modules for the signal, power, and ground wires. Low-pass filters are constructed on a breadboard, and are then connected to video baluns through a BNC connection. From the video baluns, the signal passes through a BNC to RCA connection (blue) to the USB DVRs. Green lines represent USB cables. Black dots indicate logical connections of signals and components; for true solder locations, see the instructions in the Appendices. **(B)** Conventional circuit diagram for powering and signal processing of the analog cameras, same circuit as shown in **(A)** but without illustration of cable type or spatial layout.

The filtering eliminates the crosstalk between the cameras produced by the common ground loop, but comes at the cost of losing the chrominance signal and the high frequency portion of the luminance signal. Therefore, color information is lost and a reduction in the luminance of the signal causes a dimming of the video. The drop in luminance can be compensated for by increasing the intensity of LED illumination (by changing the value of the current-limiting resistor for each

LED to produce sufficient brightness). We found that filters using a 560 Ω resistor effectively removed crosstalk without too much dimming of the video signal, but this filtering could be affected by stray capacitance in the system and the optimal resistance value may therefore differ across implementations.

Finally, we pass the filtered signal and ground for each camera through individual video baluns (video signal isolators, Part #6) before being connected to USB video capture cards (DVRs) for digitization of the video signal. The video baluns were used to isolate a second ground loop that would otherwise normally occur at this point in this system, produced by having two paths to ground: one to the ground of the camera power supply and one to the ground of the computer.

Adjustable Two-Camera Headset

Construction

We first applied a small amount of super glue (Part #7) for strain relief between the wires at the base of the prepared camera modules so they were secured for long-term use. We then soldered an independent signal, power, and ground tether (Part #8) to each camera module. A 560 Ω resistor (Part #9) was soldered at this location to the power wire, as well as an additional wire to the ground tether, for powering an illumination LED (see below). Shrink tubing was then applied to these three junctions (Part #10). For some experiments, a 6 mm collimating lens (Part #11) was placed onto the front of each camera module using tape (Part #12), but this is unnecessary and not recommended due to the additional 125 mg weight imposed. We then wrapped the camera module with a layer of micropore surgical tape (Part #13) and applied a thin coat of super glue across the surface of the tape.

For adjustable headsets that mounted independently of the headstage, we prepared two 15G hypodermic tubes to a length of 5 mm, and a 20G stainless steel wire (Part #14) to a length of 3 cm. The hypodermic tubes were inserted onto the front two screws of an assembled implant (3 in Figure 2Ai), and the stainless steel wire was cemented between them with super glue, followed by a layer of dental acrylic. For adjustable headsets that mounted with the headstage, we trimmed down a camera carrier (Part#5) using wire cutters, such that only the headstage connector and wire weaving lattice remained. We then placed 20G stainless steel wires through a weaving window on both sides of the carrier and cemented them into place. Once the wires had fully cured in place, we then cemented the two camera modules bilaterally to the stainless steel wires.

For epi-illumination of the eyes, we then cemented 3 mm IR LEDs (Part #15) to the sides of each camera module in a coaxial fashion, and soldered the leads to the power (through the current-limiting resistor) and ground tethers. Supplementary Video 7 shows an example of the video signal that is produced if epi-illumination from an attached IR LED is not utilized. For iBip headsets, we instead prepared wire soldered to the female end of electrical connectors (Part#47), and soldered the free end of this wire to the available free ends of the ground wire and powering resistor of a camera module. The wire was cut to a length to allow the male ends of these connections to be reversibly attached to the connectors of the iBip implants during experiments to power the implanted LED.

Powering and Signal Conditioning

The distal ends of the camera signal, power, and ground tethers were then soldered back to their original connections on the factory-provided wiring harness with the power and video

connectors. The two cameras were then each powered with an independent 12V DC power supply and connected with RCA cables to USB video capture cards (DVRs, Part #16) for digitization of the video signal. The factory-provided power connector includes a step-down from 12 to 3.3 V.

Data Acquisition and Processing

Electrophysiology and accelerometer signals were acquired from an attached Intan headstage amplifier (Part #17) with an RHD2000 USB interface board (Part #18) using OpenEphys software (Part #19). The Intan headstage contains 3 integrated accelerometers. We identified single neurons offline using Kilosort spike sorting software (Part #20).

For either headset design, DVRs were connected to a recording PC, and video signals were acquired with Bonsai software (Part #21) at 30 Hz and a resolution of 1,280 × 960. Video from additional webcams (Parts #22, 23) were also simultaneously acquired with Bonsai at 30 Hz and a resolution of 1,280 × 960 or 1,920 × 1,080. We increased the brightness of the ear-facing and overhead camera videos using the color balance function in Bonsai. Video can also be flipped or rotated at this point; for example, we rotated the signal from the forward camera video to compensate for the installation orientation. We also used Bonsai to record timestamps for all captured frames and log them to individual csv files for each camera. To synchronize the video signals with electrophysiology and accelerometer signals, we positioned an IR LED in view of the webcam, and drove it with TTL pulses also recorded by the RHD2000 USB interface board. The LED pulses were detected online during data acquisition with Bonsai in real time. The analog camera modules are not directly triggerable. We note that the DVRs are susceptible to electrical interference, e.g., from nearby power supplies or equipment that can introduce artifacts into the digitized video signal if too close to the DVRs.

The RS-306 camera produces an NTSC analog waveform encoding 4:3 aspect ratio interlaced frames with an optical resolution of 800 × 480 at 30 Hz. We deinterlaced the video offline to remove combing artifacts and recover the full 60 Hz field rate. Analog video is interlaced such that each 30 Hz video frame consists of two 60 Hz fields taken in sequence: the first containing the odd lines of the image, and the second containing the even lines. We used a line-doubling deinterlacing algorithm to separate each frame into two consecutive deinterlaced images consisting of the odd or even field lines, and doubled line width to preserve image dimensions, yielding deinterlaced video at 60 Hz, with an effective single-frame optical resolution around 800 × 240. The horizontal and vertical angles of view are 60° and 45°.

Stereo audio recordings for vocalization experiments were obtained with two Brüel and Kjær 1/4-inch microphones (Part #24) and acquired with a Lynx 22 sound card (Part #25) and Audacity software (Part #26). The transducers of the microphones were positioned at the ends of the cage and angled at 45 degrees to point at the base of the interaction barrier. We delivered white noise bursts through a free-field speaker at the beginning and end of each experiment along with a TTL pulse to an IR LED and the RHD 2000 interface board to synchronize audio and video recordings with electrophysiology and accelerometer signals. For the spectrograms in Figure 3B, we included noise reduction processing in Audacity using a noise profile of 5 s, noise reduction of 19 dB, sensitivity of 24, and frequency smoothing of 12.

Implants

We tapped the three holes at the front of the implant base (Figure 2Ai, Part #27) with a 00–80 tap, and cut a 00–80 screw (Part #28) to an 8 mm length and screwed it into the center hole (marked 1 in Figure 2Ai) with a washer (Part #29) to serve as a drive screw. We then tapped a 6

mm piece of plastic to serve as a cuff, and mounted it onto the end of the drive screw to create a total height of 1.3 cm from the bottom of the cuff to the top of the drive screw. For iBip implants, an IR LED (Part#15) was cemented to the bottom of the cuff, between the power and ground leads of the LED. The addition of the LED adds 5 mm in height to the implant, and therefore the drive screw and plastic cuff were instead cut to 5 and 4 mm, respectively, to achieve the total height of 1.3 cm.

For tetrode implants, we then inserted two 6 mm 18G hypodermic tubes into the center of the implant base (marked 2 in Figure 2Ai) to serve as guide rails for vertical travel of the base when advancing the electrodes. Two additional 8 mm 00–80 screws were screwed in the remaining holes at the front of the implant base (marked 3 in Figure 2Ai) from the bottom up, to serve as a site for attaching the camera headset if an independent camera attachment site was desired. For iBip implants, electrical connectors (Part#47) were placed in these holes instead, with the female connection site flush with the top surface of the implant, to serve as the connection sites to power the LED during experiments. We then soldered the power lead of the LED to the right connector, and the ground lead to the left connector. Exposed wire and solder were then coated with cement.

For tetrode implants, we inserted two 6 mm 29G hypodermic tubes through the hole in the base (marked 4 in Figure 2Ai), and cemented them in place with dental acrylic. For stainless-steel wire arrays, we inserted 7 mm 19G hypodermic tubes and cemented them in place with dental acrylic near their relative stereotactic locations on the implant base to accommodate two teflon-coated stainless steel wires each (Part #30).

We used small EIB pins (Part #31) to electrically connect individual stainless steel wires to the ground and reference channels on a Neuralynx EIB (Part #32). An EIB (electrode interface

board) is a miniature break-out board with a headstage connector (such as an Omnetics connector) and connection points for implanted microwires, to provide a robust interface between a headstage and electrode or tetrode channels. The remaining channels on the EIB were similarly connected to prepared tetrodes (Part #33) or stainless steel wires for tetrode and wire-array implants, respectively. Once connected, we coated these sites with silicone sealant (Part #34). The reference and ground wires were either routed through the drive posts for tetrode implants, or two 19G hypodermic tubes in the case of wire-array implants. The tetrodes or remaining stainless-steel wires were then routed through their respective hypodermic tubes, and the EIB was lowered and flushly screwed into place on the surface of the implant base with two screws (Part #35). Stainless steel wires routed through the same tubes were cut to slightly different lengths so that we could properly identify them during implantation and note their respective channels on the EIB. The implants were then sterilized in 70% EtOH before implantation. Protective caps (Figure 2Aii, Part #36) were attached to implants after surgery.

Surgery

All procedures were performed in accordance with National Institutes of Health guidelines, as approved by the University of Oregon Institutional Animal Care and Use Committee.

For the experiments described here, we used adult C57bl/6 mice (n = 9, both males and females, >3 months of age, weighing 18.5–31 g at the time of surgery) and made craniotomies as described below; these can be customized to the specific needs of different experiments. Mice were anesthetized with isoflurane (1–2%). A craniotomy was created over the right hemisphere, where a skull screw (Part #37) was fastened into place and cemented with dental acrylic. Two additional craniotomies were then created at −1.5 AP, −2 ML, 0 DV, and −2 AP, −2 ML, 0 DV

for the ground and reference wires. For implants utilizing infrared back-illumination pupillometry [iBip; (Yüzgeç et al., 2018)], a 2 mm craniotomy was created at 4 AP, 0 ML, 0 DV relative to bregma, and a coverslip was secured overtop using vetbond. For tetrode implants, a small craniotomy was created dorsal to anterior lateral motor cortex (ALM) at 2.5 AP, 1.5 ML, 0 DV (relative to bregma). For wire-array implants, craniotomies were similarly created for recordings in the olfactory bulb at 4.5 AP, 0.8 ML, 0 DV, ALM at 2.5 AP, 1.5 ML, 0 DV, anterior cingulate cortex (ACC) at 1.98 AP, 0.35 ML, −1.8 DV, CA1 of the hippocampus at −2.06 AP, 1.5 ML, −1.5 DV, the barrel field of primary somatosensory cortex (S1BF) at −1 AP, 3.5 ML, 0 DV, secondary somatosensory cortex (S2) at −1.5 AP, 4.5 ML, 0 DV, primary auditory cortex (A1) at −2.9 AP, 4.5 ML, 0 DV, and secondary auditory cortex (A2) at −2.5 AP, 4.2 ML, 0 DV. Sterile saline was immediately applied and maintained at these locations to prevent drying of the dura.

Proper positioning of the cameras, electrodes, and other hardware such as optical fibers or microinjection ports will depend on the body parts and brain areas being targeted. For the experiments described here, EIBs were stereotactically placed with the center of the surface of their base at −5.5 AP, 0 ML, 10 DV from bregma. This was achieved with the fixed dimensions of the implant by positioning the drive screw (or the IR LED in the case of iBip implants) at 4 AP, 0 ML, 0 DV relative to bregma, and ensuring the total height of the implant was 1.3 cm from the bottom of the cuff (or the IR LED in the case of iBip implants) to the top of the drive screw. This positions the EIB centrally over the head and the camera carrier such that the cameras are over the ears and the front of the head.

For tetrode implants, the tetrodes were trimmed at this point so they would pass just beyond the level of the dura when the implant was lowered into its final position. Once at the proper length, we applied a thin coating of antibacterial ointment to the tetrodes, made a small incision in the dura, and slowly lowered the implant and tetrodes into place. We then coated the remaining exposed portion of the tetrodes in vaseline, and cemented the vaseline, cuff, and surrounding surface of the skull with dental acrylic. We then positioned the ground and reference wires just below the dura in their respective craniotomies, and cemented them with dental acrylic along with the drive posts so that no portion of the wires were left exposed.

For wire-array implants, the stainless steel wires were splayed out laterally so the implant could be lowered into its proper position. We then raised the implant 1.5 mm dorsally, and positioned the hippocampal wire vertically just above the dura, and cemented it to the hypodermic tube in this position with dental acrylic. This process was then repeated for the remaining electrodes targeting non-superficial structures. We then made small incisions in the dura at these locations, and slowly lowered the implant into position. We applied dental acrylic to these two sites and the cuff to cement them in place. Once the acrylic sufficiently stabilized the implant, the remaining wires were placed just below the dura in their respective craniotomies, and cemented with dental acrylic so that no portion of the wires were left exposed.

We administered Ketoprofen (5 mg/kg) to reduce post-operative inflammation. The bottom surface of a protective cap (Part #36) was then coated with silicone sealant (Part #34) and snapped over the EIBs of the implant to cure in place. Mice were then given 7 days of post-operative recovery.

Experimental Conditions

All experiments occurred within an electrically shielded sound-attenuating chamber. Sleep experiments occurred in the nest of the home cage, with no external sources of illumination. Vocalization experiments occurred in the home cage of individually housed male mice. A webcam (Part #22) recorded video directly above the arena (referred to as the "SkyCam"), with illumination from an IR LED light source (Part #38) and 6000K LED Floodlight (Part #39). We placed a perforated clear acrylic barrier (Part #40) between the resident male, who was unimplanted, and an implanted female. Vocalizations were recorded with two overhead Brüel and Kjær 1/4-inch microphones (Part #24).

Prey capture experiments occurred in a 24 inch diameter circular arena with a clean paper floor. SkyCam video of the arena was recorded as described above. Illumination was provided by an IR LED light source (Part #38) and 5,500 K lightbulb (Part #41). An implanted mouse waited in the arena until a cricket was remotely dropped into the arena, and then the mouse chased and captured the cricket (Hoy et al., 2016).

Free field exploration experiments occurred in the same arena as prey capture experiments. We used a webcam (Part #22) to record from one side of the arena, and a dome camera (Part #23) to record from above, with illumination provided by an IR LED light source (Part #42) and 6000K LED Floodlight (Part #39).

Bridge to Chapter III

In this chapter, I have presented a novel head-mounted camera system allowing large-scale electrophysiological recordings to be paired with multi-camera headsets for simultaneous behavioral monitoring in freely moving mice. In Chapter III, I utilize this system to identify

distinct behavioral movements of the nostrils and ears in freely moving conditions, and incorporate cortex-wide electrocorticography to identify large-scale spatiotemporal motifs of cerebral theta oscillations underlying natural behavior.

Supplementary Video Legends

Supplementary Video 1. An example video of the four-camera headstage-integrated headset showing the dynamic activity of the rhinarium, whiskers, eyes, and ears of a freely moving mouse. Panels show the webcam views of a mouse from the side (top left) and above (top right), and the video signals from the four-camera headstage-integrated headset: left ear camera (bottom left), right ear camera (bottom right), overhead camera (bottom middle), and forward-facing camera (top middle). Note that the overhead camera video signal is of higher quality than the front-facing or ear-facing videos, due to their filtering.

Supplementary Video 2. An example video showing rasters of unit activity from six cells in anterior lateral motor cortex (ALM) (bottom) during prey capture behavior (a mouse chasing and capturing a cricket). Traces from the accelerometer channels are shown below. Spikes from cells 1, 2, 4, and 6 are plotted in real time (waveforms at top) and indicated in the audio by 50 ms tones of 800, 1,200, 1,400, and 1,600 Hz, respectively.

Supplementary Video 3. An example video of courtship behavior. A spectrogram (top) shows ultrasonic vocalizations as they occur during the video of the behavior shown below. Continuous LFP traces from 8 brain regions are shown below. Audio was pitch shifted in audacity to bring the vocalizations within the frequency range of human hearing. Note that this spatial arrangement of the cameras leaves ample room for mice to utilize the nosepoke ports of the interaction barrier.

Supplementary Video 4. Three example videos showing several epochs of natural cyclotorsion of the eye using the three different compositions of headset components shown in Figure 4 (with/without collimating lens, epi-illumination, and back-illumination). Optical conditions are listed before each example. Playback speed was 0.25x.

Supplementary Video 5. An example video using this system with infrared back-illumination pupillometry (iBip), which reveals the fundus and optic disc as the eye moves its position within the orbit of an awake freely-moving mouse. A cropped portion of the raw deinterlaced video (left) is shown with its inverse image (right) for clearer visualization of the fundus. A whisker between the camera and the eye happens to move in and out of frame throughout the video. The full-frame (uncropped) inverse image video follows at the end of the video. See Supplementary Video 4 for an iBip example showing the whiskers in white light, and Supplementary Video 6 for examples of iBip across sleep-wake cycles in the dark.

Supplementary Video 6. Example videos showing behavior across the sleep-wake cycle of an unrestrained mouse in the nest of the homecage using this system with iBip. Wake is shown in real-time, and is characterized by a large pupil diameter, and active movements of the eyes, whiskers, and limbs. NREM sleep is shown at 20x speed, and is characterized by immobility and slow large amplitude fluctuations of the pupil. Putative REM sleep is shown in real-time, and is characterized by a small pupil diameter and active twitching of the eyes, whiskers, and mystacial pad occurring during a background of immobility.

Supplementary Video 7. An example video showing the pupil and whiskers during the natural jumping behavior of a freely-moving mouse. Using the adjustable mounting system, different positions can be tested for pilot experiments without having to iteratively rebuild headsets (compare the different camera angles in Supplementary Videos 2, 7). This video also shows an example of the video signal obtained without an integrated IR LED (note how the illumination varies as the mouse moves relative to the overhead lighting).

CHAPTER III

BRAIN-WIDE SPATIOTEMPORAL MOTIFS OF THETA OSCILLATIONS ARE COUPLED TO FREELY MOVING BEHAVIOR

This chapter includes unpublished co-authored material. Nicholas J. Sattler performed experiments; Nicholas J. Sattler and Michael Wehr analyzed data and interpreted results; Nicholas J. Sattler prepared figures; Nicholas J. Sattler and Michael Wehr wrote the manuscript.

Introduction

How are neural activity and computation coordinated across the brain, and how does this underlie behavior? Recent studies have highlighted the existence of prominent movement-related signals throughout the brain (Schneider and Mooney, 2018; Musall *et al.*, 2019; Stringer *et al.*, 2019; Parker *et al.*, 2020). This widespread activity likely reflects the integration of sensory processing with ongoing movement, as animals interact with and actively sample the sensory environment during natural freely moving behavior. In the broader context of brain function, processes such as sensorimotor integration, decision-making, and memory rely on the ability of neural circuits to communicate flexibly and efficiently across widespread brain regions. Although local and long-range connections undoubtedly provide the anatomical substrate for this communication, it is less clear whether anatomical connections can meet the demands of dynamic and flexible communication required for the rapid timescale of natural behavior. Coherent oscillations have been proposed as a possible mechanism for such flexible routing of information across brain regions (Fries, 2005).

Oscillatory brain activity occurs across a wide range of frequencies, but the hippocampal theta rhythm (4-12 Hz) is especially prominent, and has been linked to locomotion and exploratory

behavior in many species from rodents to humans (Buzsáki, 2002; Aghajan *et al.*, 2017). In particular, hippocampal theta plays a key role in sensorimotor integration, spatial navigation, and memory formation, and coordinates neuronal spiking in other brain regions such as frontal cortex (Hyman *et al.*, 2005; Jones and Wilson, 2005a, 2005b; Siapas, Lubenov and Wilson, 2005; Benchenane *et al.*, 2010; Kim, Delcasso and Lee, 2011). The theta rhythm is not synchronous across the hippocampus, but rather forms a traveling wave along the septotemporal axis (Lubenov and Siapas, 2009; Patel *et al.*, 2012; Zhang and Jacobs, 2015). Traveling theta waves have also been observed in human intracranial cortical recordings, where they are related to memory encoding and recall (Bahramisharif et al., 2013; Zhang et al., 2018; Mohan et al. 2024). However, it remains unknown whether coherent theta oscillations occur over the entire neocortex, whether they are spatiotemporally organized into traveling waves, or how they are related to behavior.

Recent studies have demonstrated that cortical activity exhibits metastable dynamics, in which brain activity unfolds as a sequence of discrete quasi-stationary states that are separated by abrupt transitions (La Camera, Fontanini and Mazzucato, 2019; Recanatesi *et al.*, 2022). For example, spatiotemporal patterns of gamma oscillations across the cortex appear to occur in bouts, which contain stimulus information and are separated by brief transitional periods of low-amplitude, asynchronous activity that have been termed “null spikes” (Freeman, 2007; Kozma and Freeman, 2017). Metastable state sequences of cortical spiking patterns conveying stimulus information have similarly been observed across species, and are theorized to allow neural computations to proceed along a sequence of distinct epochs, in which brain activity forms quasi-stable neural representations punctuated by rapid state transitions (Abeles *et al.*, 1995; Jones *et al.*, 2007; Ponce-Alvarez *et al.*, 2012). With a lack of direct recordings across the cortex however,

whether metastable dynamics occur for traveling waves of theta oscillations, or what the spatial extent of the metastable states may be, has remained theoretical (Roberts *et al.*, 2019; Cabral *et al.*, 2022).

To investigate these spatiotemporal dynamics at a brain-wide scale, we recorded field potentials using a large-scale electrocorticography (ECoG) array covering nearly the entire dorsolateral surface of the brain in freely moving mice. We found prominent theta oscillations that were spatiotemporally organized into three major bilateral traveling waves that were strongly modulated by mouse running speed. These three patterns showed metastable dynamics, alternating during transient desynchronization events that induced a phase reset in the dominant traveling wave pattern. These brain-wide spatiotemporal patterns of oscillatory activity could serve to integrate sensory, cognitive, and behavior information that is distributed across the cerebral cortex.

Methods

Electrode arrays and headset

For all electrodes, stainless steel 000-120 flathead slotted drive screws (Antrin Miniature Specialties) were soldered to 42 mm long teflon-coated stainless steel wire (A&M systems, recording electrodes: 790500 50.8µm diameter, ground and reference electrodes: 791400 127µm diameter) and pinned to a 32-channel electrode interface board (Neuralynx 31-0603-0127). Reference and ground channels were soldered to one common screw. Impedances were confirmed to be within the range of 1-3Ω for the ground and reference channels, and 16-17Ω for the recording channels. The spatial layout of the electrode array was adapted from the epicranial design of (Mégevand *et al.*, 2008), with the inter-electrode distance increased to 1.8 mm, to fully span the cortex when curved over its surface. A stencil of electrode locations was laser-cut from filter paper

(Whatman 1001-185), for use during surgery. The carrier headset for head-mounted camera arrays (Sattler and Wehr, 2020) was mounted to a 32-channel headstage (Neuralynx #C3324).

Surgical procedure

Mice were anesthetized with isoflurane (1.5%). The electrode array stencil was aligned to bregma, flattened over the skull, and used to mark electrode locations on the surface of the skull. Craniotomies were then created over each electrode location to fully expose the dural surface, and the electrode was fastened into place and covered with dental acrylic. Mice were housed individually after surgery, and allowed at least a week of postoperative recovery before recordings.

Animals and experimental procedure

We recorded from b6 mice (N = 3 mice, 2 male, 1 female). Experiments were performed in an electrically shielded sound-attenuating chamber. Mice were placed in a 60 cm diameter cylindrical arena for 2 exploration sessions a day (1 in the dark (5 minutes) and 1 in the light (5 minutes)) for 6 days. Mice were food restricted for the last three days (1 hour of access to food per day, after their sessions). Mice were active for all sessions (locomoting or rearing), with rare periods of grooming or behavioral quiescence. Sessions were halted if the tethers of the mouse became tangled, and were resumed for the remaining time in each session once the tethers had been untangled.

Data acquisition

Continuous data was recorded at 30 kHz sampling rate using a 32-channel headstage (Intan Technologies #C3324), USB interface board (Intan Technologies RHD2000 board), and Open Ephys software (Siegle *et al.*, 2017) with a digital bandpass filter of 2.4959 to 7603 Hz. The overhead camera (FLIR BFS-U3-16S2M) was captured at 200 Hz, and the head mounted cameras

were captured and deinterlaced at their 60 Hz field-rate using Bonsai. Signals were synchronized using illumination of an IR LED from TTL pulses as described in (Sattler and Wehr, 2020).

Behavioral tracking

All behavioral data was tracked using DeepLabCut (Mathis *et al.*, 2018). From the overhead camera, six points on the head-mounted camera headset of the mice were used to calculate their bearing in the arena, and a point on the back of their neck was used to calculate their speed. From the mounted head camera, the left and right nostrils were tracked, and their bearing relative to the mouse's midline were calculated. From the ear cameras, a distinct point on the posterior edge of the pinna was tracked, and their bearing relative to the mouse's midline were similarly calculated.

Pre-analysis

For all analysis, the raw continuous data was first bandpass filtered at 1 to 30 Hz using a 1st order butterworth filter (implemented using *filtfilt.m* in Matlab), and downsampled to 200 Hz to facilitate data processing while retaining high fidelity. All behavioral measurements from the cameras were similarly resampled at 200 Hz. For two mice, a dead channel was interpolated from neighboring channels prior to downsampling. Sessions which contained an instance of a large electrode artifact (4 sessions from 1 mouse) were excluded from analysis.

Analytic signals

Data was filtered at 9 Hz using wavelet-based filtering (implemented using *wFilter.m* from Matlab Central File Exchange), with a bandwidth of 1 standard deviation of the wavelet's gaussian function, and converted into analytic signals using a Hilbert transformation.

Order parameter (r) was calculated as:

$$r = \left| \frac{1}{N} \sum_{j=1}^{N} e^{i\theta_j} \right|$$

where N = number of oscillators, and θ = phase. Null spikes were detected by identifying periods in which the absolute value of the change in order parameter exceeded 0.015/s.

Singular value decomposition

Singular value decomposition (SVD) was performed on the complex-valued analytic signals extracted from the theta-filtered LFPs to produce eigenmodes of oscillatory activity as follows:

$$A = U\Sigma V^*$$

where A is an n by t matrix of n analytic signals at t timepoints, U is an n by n complex-valued matrix where each column represents the eigenvectors, Σ is an n by t diagonal matrix containing the singular values for each eigenvector, V is a t by t complex-valued matrix where each row represents the eigenvalues at each timepoint for each eigenmode, and $*$ represents the Hermitian transposition.

Additionally, an arbitrary "reference" channel was chosen after decomposition to align each eigenvector (and associated eigenvalues) to a common phase angle. We chose the right posterior channel of retrosplenial cortex (-4.2288 AP, +0.9 ML), and rotated each eigenvector (and their respective eigenvalues) as follows:

$$z_{new} = z_{old} e^{-i*\phi_{ref}}$$

where z_{old} is the original complex-valued eigenvector (or eigenvalue), ϕ_{ref} is the initial phase angle of the reference channel of the eigenvector, and z_{new} is the resulting complex-valued eigenvector (or eigenvalue). This therefore aligned the eigenmodes such that the chosen reference channel was at a phase angle of 0, and shifted their respective eigenvalues appropriately.

A relatively continual decrease in percent variance explained was observed for modes 2 and beyond, with no abrupt drop off. Analysis was limited here to the first 3 modes, as the patterns of modes 4 and beyond were variable across the mice.

Spatial phase gradient

Spatial phase gradients were calculated for each channel using its set of nearest neighbors, and therefore consisted of a scalar value (rads/mm) for each of the three spatial components of the hexagonal lattice: x (-π,0), y (-2π/3,π/3), and z (-π/3,2π/3). Phase derivatives were taken for each of these components by taking the angle of the product of the analytic signal with the complex conjugate of the second, using the forward or central difference when available. Vector summation of these three components was then used to calculate the resultant vector. To calculate curl, the spatial vector field was interpolated into a 15x15 matrix, and quantified using *curl.m* in Matlab.

Results

Theta oscillations are prominent across the cortex

We recorded local field potentials (LFPs) across the dorsolateral surface of the cortex using a 31-channel ECoG array (Figure 1A) while mice (N = 3) freely explored an open arena (Figure 1B). To monitor fine movements of the ears, nose, and face under freely moving conditions, we used an array of 3 head-mounted cameras (Figure 1B; (Sattler and Wehr, 2020)). LFP signals recorded from all channels and cortical regions exhibited a distinct peak in the theta range (Figure

1C,D). These theta oscillations showed pronounced phase differences across the cortical surface, consistent with a traveling wave. The instantaneous spatial phase gradient of theta-filtered LFPs (Figure 1E, time point corresponding to the vertical line in Fig. 1D) typically showed a divergent traveling wave. This indicates that moment-to-moment theta oscillations show brain-wide spatiotemporal structure.

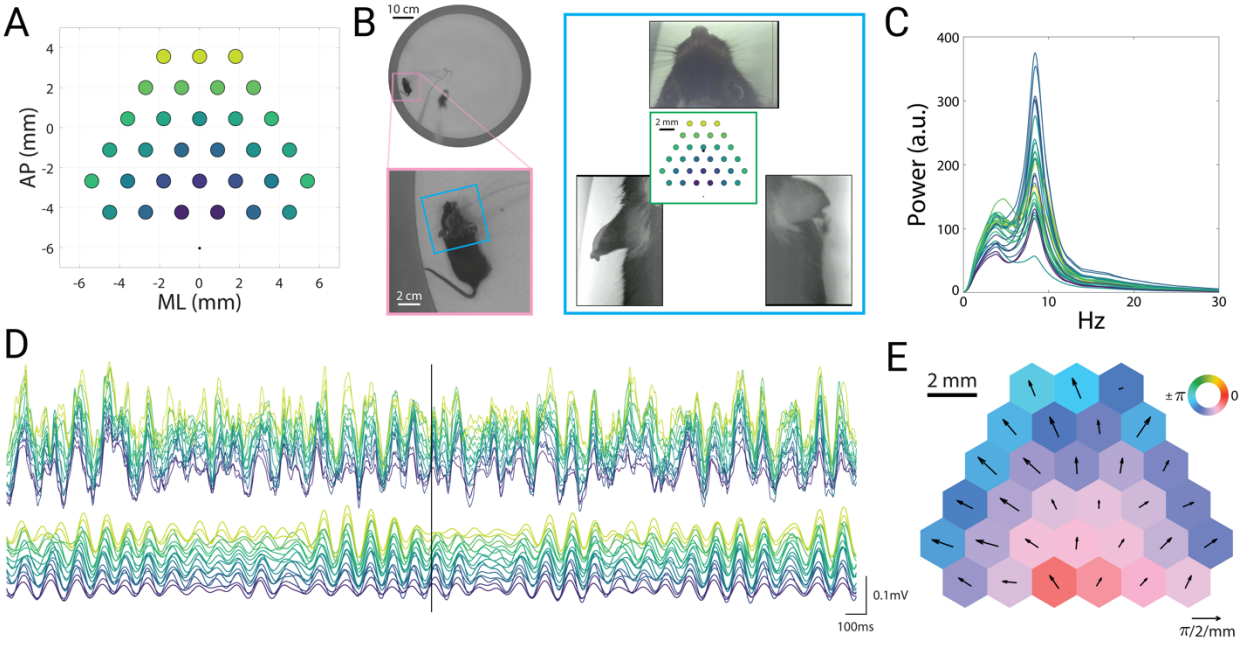

Figure 1. Theta oscillations are prominent across the cortex.
(A) Geometry of the electrocorticography (ECoG) array, showing actual electrode size (0.8mm) and inter-electrode distance (1.8mm). Black dot indicates the reference electrode location. AP and ML values indicate inter-electrode distances along the curved surface of the skull, relative to initial alignment with bregma, and do not represent conventional 2D stereotactic coordinates. Colors indicate electrode position and correspond to channel colors in C-D. **(B)** Top view of the arena (top left), with inset showing an enlarged view of the mouse (bottom left). Overhead view of the head and ears from head-mounted cameras (right), with the ECoG array overlaid in the center. **(C)** Power spectral density for each channel. Signals were band-pass filtered 2.5-30 Hz. **(D)** Example recording traces of the local field potentials (top) and theta-filtered signals (9 Hz, bottom). Vertical black bar corresponds to the time point shown in panels B and E. **(E)** Instantaneous phase (colors) and spatial phase gradient (quivers) of the theta-filtered signals at the time point indicated by the black bar in panel D. Hexagonal tiles indicate electrode relative position but not actual size or shape.

This instantaneous snapshot of a brain-wide traveling wave (Fig. 1E) closely matched the long-term average of the signals. The spatial phase gradient of these oscillations averaged across sessions and mice appeared as a bilaterally divergent vector field that originated in posterior retrosplenial cortex (Figure 2A, top). The mean amplitudes also showed a bilaterally symmetric pattern, with the highest theta amplitude in anterior retrosplenial cortex, roughly above the hippocampus (Figure 2A, bottom). Thus, both instantaneous and long-term average of these oscillations appeared as a global traveling wave. We wondered whether this traveling wave was stable over time, or showed dynamics that might relate to ongoing behavior. To address this, we turned to spectral decomposition methods to characterize spatiotemporal activity patterns.

Theta oscillations can be decomposed into cortical modes

To identify distinct spatiotemporal motifs of oscillatory activity, we used complex-valued singular value decomposition to extract oscillatory "modes" (eigenvectors), that is, specific spatiotemporal patterns consisting of fixed amplitude and phase relations among the channels. This analysis revealed three prominent modes (Figure 2B), which collectively represented roughly 50% of the variance in the dataset, and were consistent in power across both illuminated and dark arena conditions (Figure 2C).

The most prominent mode ("Mode 1") strongly resembled that of the mean amplitude and phase gradient, and represented around 40% of the variance (Figure 2C). This oscillatory mode was not synchronous across the cortex, but rather showed a smoothly varying pattern of phase lags that formed a bilaterally divergent traveling wave originating near posterior retrosplenial cortex. In contrast to this pattern, the following two modes (Modes 2 and 3) were fully asynchronous

(containing phase angles across the entire unit circle), with spatial phase gradients that formed bilateral spirals centered roughly over somatosensory cortex (Figure 2B).

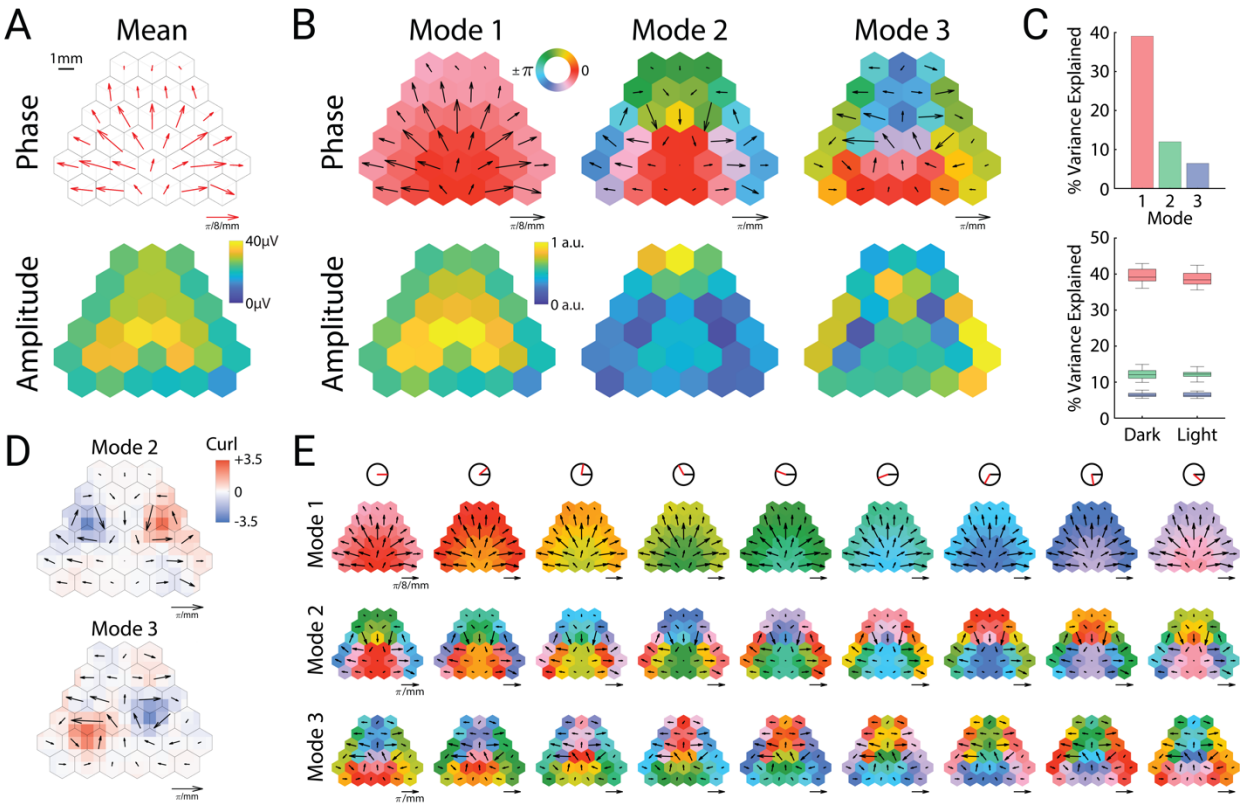

Figure 2. Theta oscillations can be decomposed into cortical modes
(A) Mean spatial phase gradient (top) and amplitude (bottom). **(B)** Phase (top row) and amplitude (bottom row) of the three prominent cortical modes. **(C)** Variance explained by each mode across all sessions (top) and between dark and light sessions (bottom). Upper and lower portions of the box plots correspond to the upper and lower quartiles respectively. The middle lines correspond to the median value, and error bars correspond to minimum and maximum values. **(D)** Vector curl calculated on interpolated values of the spatial phase gradients for modes two and three. **(E)** Cortical cyclograms showing the progression phase along their spatial phase gradients across one full cycle (from left to right). The red line in the top row indicates the current phase angle of the column.

To quantify these spiral patterns, we computed the vector curl of Modes 2 and 3, which revealed strong bilateral singularities of opposite rotational directions (Figure 2D). Modes 2 and 3 differed in that Mode 2 was clockwise in the left hemisphere, whereas Mode 3 was counterclockwise (and vice versa). Similar to smaller mesoscopic spiral waves that have been

previously observed in rodent (Huang *et al.*, 2004, 2010) and human (Xu *et al.*, 2023) neocortex, the lowest amplitudes were observed near the phase singularity for both modes. Mode 2 displayed high amplitude in frontal cortex, whereas Mode 3 displayed high amplitudes in the temporal and parietal poles of the cortex (Fig. 2B).

The bilateral phase symmetries of both Modes 2 and 3 result in opposite rotational directions of the left and right spirals. The temporal sequence of the phase gradient can therefore be described relative to the midline for both hemispheres. In the case of Mode 2, the phase sequence flows in a lateral → anterior → medial → posterior sequence, whereas Mode 3 flows in an anterior → lateral → posterior → medial sequence. Cortical cyclograms illustrate how the phase sequence modes unfold in time through a full theta cycle (Figure 2E).

Modes are interrelated and correlate with mouse speed

The spatiotemporal motifs shown in Figure 2 represent time-averages across all recording sessions and mice. How do these modes unfold in time? To investigate the dynamics of these modes, we measured the instantaneous mean amplitude across all channels as a measure of overall cortical power, and the order parameter as a measure of synchrony across channels. The order parameter (see Methods) is a vector strength measure that varies from 0 (complete asynchrony) to 1 (complete synchrony).

A comparison of mean amplitude and order parameter over a representative ten-second period (Figure 3A top) along with the three modes (Figure 3A bottom) reveals strong relationships between these measures. Mean amplitude typically remained high for periods of roughly 1 second, and these periods were often punctuated by brief drops in amplitude. These dips in amplitude were tightly associated with sharp drops in the order parameter, indicating that global theta oscillations

alternate between stable periods of high amplitude and synchrony, interrupted by brief events during which the amplitude and synchrony dropped to very low values. Similar brief desynchronization events have been previously described in ECoG recordings of gamma-band activity from local brain regions such as visual cortex or olfactory bulb, for which Walter Freeman coined the term "null spikes" (Freeman, 2007; Kozma and Freeman, 2008). Although mean amplitude and order parameter showed distinct distributions (Figure 3B), cross-covariation analysis revealed that amplitude and order parameter were highly correlated with each other (Figure 3C), as expected from the large and tightly coordinated impact of null spikes on both measures. Moreover, Mode 1 was strongly correlated with order parameter and mean amplitude, whereas Modes 2 and 3 were anti-correlated with these measures (Fig. 3C).

The joint probability distribution of order parameter and mean amplitude shows that theta oscillations dwelled for most of the time at moderate levels of amplitude and synchrony (Figure 3Di), in which Mode 1 dominates (Figure 3Dii). Brief periods when theta activity plunged into low-order and low-amplitude null spikes (Figure 3Di) were dominated by the spiral pattern of Mode 2 (Figure 3Dii). However, Mode 2 activity was not confined to null spikes, but was consistently present during stable periods as well, coexisting in superposition with Mode 1 (Figure 3Diii, iv).

Figure 3. (next page) Modes are interrelated and correlate with amplitude and synchrony
(A) Example trace of the mean electrode amplitude across channels (black), order parameter (purple), and modes 1, 2, and 3 (red, green, and blue respectively) across a 10 second period. Colors carry over across the figure. **(B)** Distributions of mean amplitude and order parameter. **(C)** Cross-covariance of the order parameter and modes (percent variance explained) with mean amplitude. **(D)** Scatter plots with overlaid occupancy values (left) and their corresponding modal compositions (right).

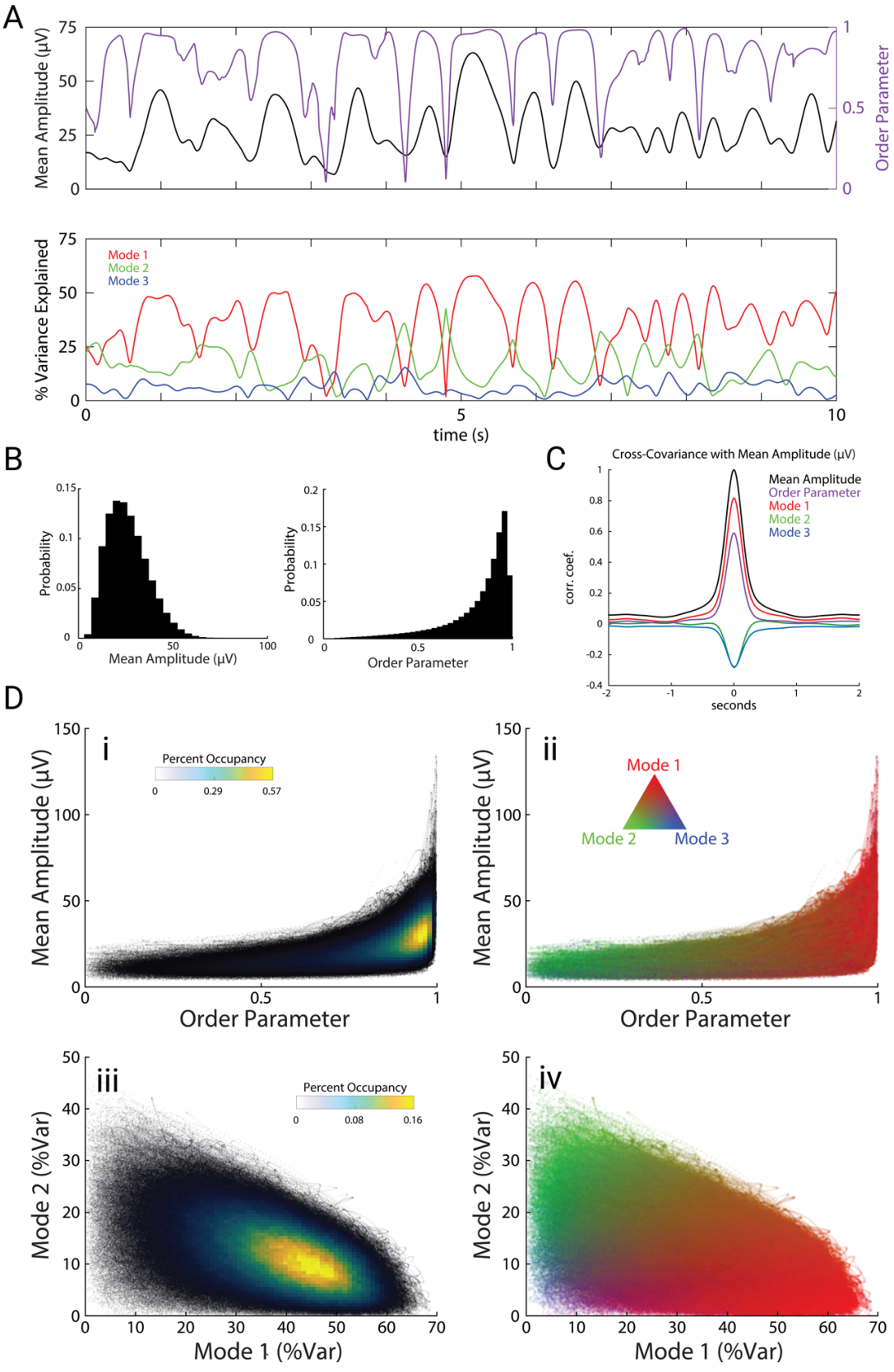
A
Mean Amplitude (μV)
Order Parameter
% Variance Explained
Mode 1
Mode 2
Mode 3
time (s)
B
Probability
Mean Amplitude (μV)
Order Parameter
C
Cross-Covariance with Mean Amplitude (μV)
Mean Amplitude
Order Parameter
Mode 1
Mode 2
Mode 3
corr. coef.
seconds
D
i
Percent Occupancy
ii
Mode 1
Mode 2
Mode 3
iii
iv
Mode 2 (%Var)
Mode 1 (%Var)

These measures of theta oscillations were tightly correlated with mouse speed during free exploration of the open arena (Figure 4A left). Specifically, mouse speed was correlated with mean amplitude, order parameter, and Mode 1. This indicates that these measures of global brain activity are related to mouse movements. In contrast to experiments with stereotyped mouse trajectories on linear tracks, open-field exploration involves wide variations in mouse speed, mouse turning, and coordinated movements of the head, ears, and nose. To investigate how these aspects of mouse movement related to theta oscillations, we first measured mouse turning, which we quantified as angular velocity ω (rads/s) of the mouse's head. Mouse turning during open exploration was tightly correlated to speed (Figure 4A). During these turning events, the movements of the ears and the nose were tightly correlated with the direction of the turn (Figure 4B). Whereas turning was correlated with speed, and speed was correlated with theta activity (amplitude, order parameter, and Mode 1), we found that turning was not correlated with any measures of theta (Figure 4A right). Ear and nostril movements were also uncorrelated with any measures of theta (data not shown). Theta activity therefore appeared to be specifically related to locomotion speed as opposed to general movements of the mouse, head, ears, or nose.

We next wondered whether the prominent fluctuations in amplitude, Mode 1, and order parameter during null spikes underlie their correlation with mouse speed. To address this question, we detected null spikes using an algorithm based on the rate of change of the order parameter (see Methods). Null spikes (N = 9212) had a mean duration of 0.140 ± 0.051 s, and the stable periods between null spikes had a mean duration of 1.156 ± 1.164 s (Figure 4C), consistent with previous reports of null spikes in theta activity recorded from local brain regions (Kozma and Freeman, 2008). Figure 4D (left) shows the stable periods between null spikes, sorted by duration, such that

the delineation of stable periods by the sharp drop in order parameter (null spikes) appears as a blue V-shaped boundary. Figure 4D (right) shows the covariance of mouse speed with three measures of theta activity (amplitude, Mode 1, and order parameter) during these stable periods. For all three measures, a positive correlation during the stable periods appears as a yellow band, and as a peak in the averaged covariance at the bottom. In contrast, mouse speed was not correlated with these theta measures during the null spikes themselves. Figure 4E shows all null spikes, sorted by duration. Covariance of mouse speed with amplitude, Mode 1, and order parameter were negligible during null spikes. This indicates that despite the large and coordinated fluctuations of amplitude, Mode 1, and order parameter during null spikes, these contribute little to the correlation between mouse speed and theta activity, which is instead driven by smaller fluctuations during the stable periods between null spikes.

Figure 4. Mode 1 correlates with mouse speed during stable periods
(A) Cross-covariance of the mean amplitude, order parameter, Mode 1, and mouse turning with mouse speed (left) and turning (right). Here we used the absolute value of angular velocity ($|\omega|$, rads/sec) to avoid cancellation of correlations between clockwise and counterclockwise turns. **(B)** Illustration of mouse nostril and ear movements (left). During a clockwise turn, we define mouse turning (ω) to be positive, and observed that motion of both nostrils strongly tended to also be clockwise (positive), whereas both ears strongly tended to move counterclockwise (negative). Cross-covariance of the nostrils and ears with mouse turning (right). Note the strong positive correlation of nostrils with turning, and the strong negative correlation of ear movements with turning (corresponding to the arrows depicted for the body parts at left). **(C)** Distributions of null spike (top) and inter-null spike durations (bottom). **(D)** Order parameter for all stable periods (N = 9212) between null spikes sorted by duration (left). Cross-covariance with mouse speed during each stable period for mean amplitude, Mode 1, and order parameter, with average cross-covariance of all stable periods plotted below (right). **(E)** Order parameter for all null spikes (N = 9212) sorted by duration (left). Cross-covariance with mouse speed during each null spike for mean amplitude, Mode 1, and order parameter, with average cross-covariance of all null spikes plotted below (right).

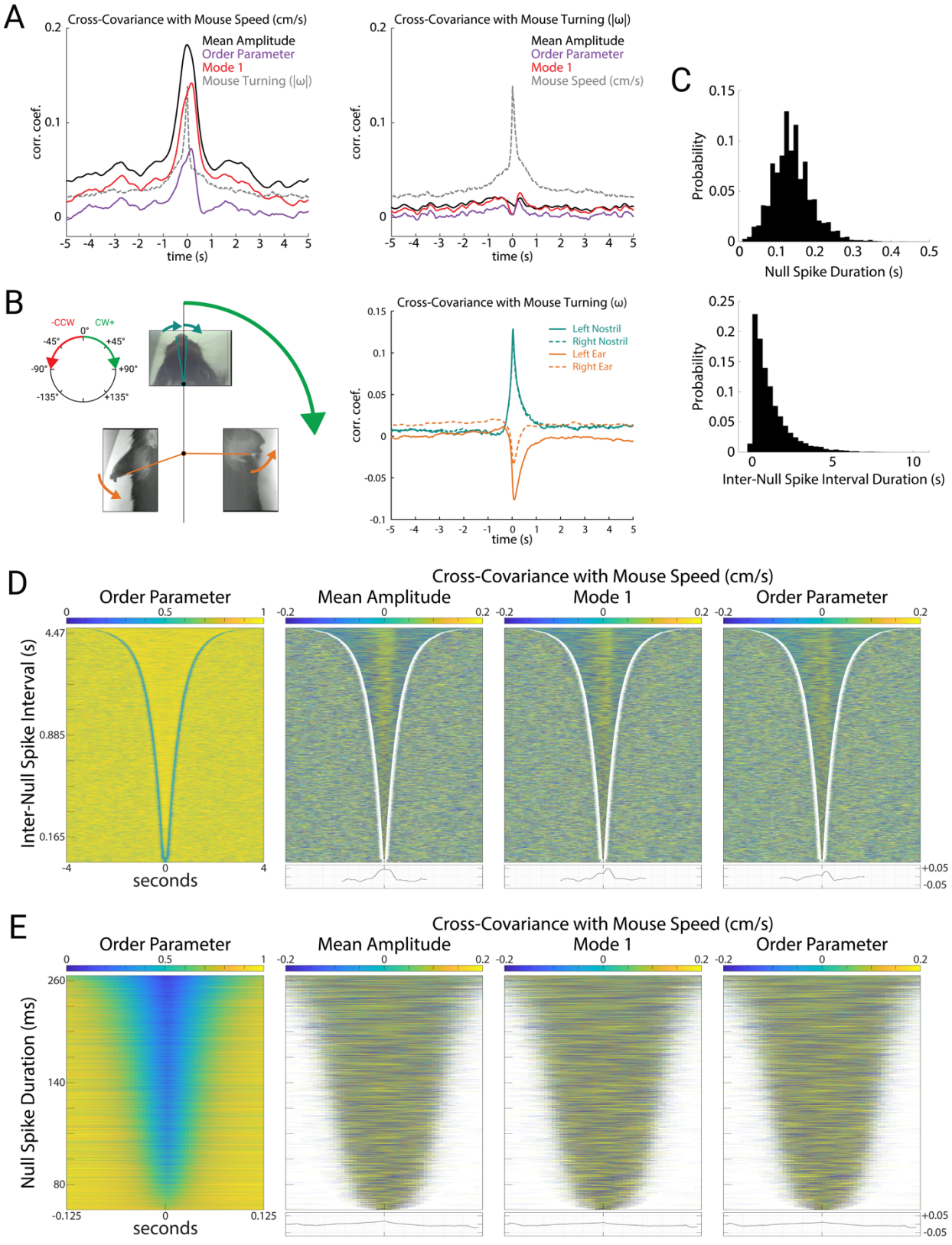
A
Cross-Covariance with Mouse Speed (cm/s)
Mean Amplitude
Order Parameter
Mode 1
Mouse Turning (|ω|)
corr. coef.
time (s)
Cross-Covariance with Mouse Turning (|ω|)
Mean Amplitude
Order Parameter
Mode 1
Mouse Speed (cm/s)
corr. coef.
time (s)
C
Probability
Null Spike Duration (s)
B
-CCW
CW+
0°
-45°
+45°
-90°
+90°
-135°
+135°
Cross-Covariance with Mouse Turning (ω)
Left Nostril
Right Nostril
Left Ear
Right Ear
corr. coef.
time (s)
Probability
Inter-Null Spike Interval Duration (s)
D
Cross-Covariance with Mouse Speed (cm/s)
Order Parameter
Mean Amplitude
Mode 1
Order Parameter
Inter-Null Spike Interval (s)
seconds
E
Cross-Covariance with Mouse Speed (cm/s)
Order Parameter
Mean Amplitude
Mode 1
Order Parameter
Null Spike Duration (ms)
seconds

Cortical null spikes impose a phase-reset of Mode 1

Cortical null spikes thus appear to be independent of the correlation between theta oscillations and behavior. We therefore wondered what role they might play in the ongoing dynamics of the spatiotemporal modes of theta oscillations. The alternation of null spikes and the stable periods between them have been previously described as “beats,” (Kozma and Freeman 2008) suggesting that they could be a form of amplitude modulation arising from destructive interference between oscillations of slightly different frequencies.

To test this hypothesis, we examined phase slip across null spikes and stable periods. If amplitude modulation arises from beating between similar stable oscillation frequencies, the phase of the oscillation should be relatively stable and unaffected by the beats. Figure 5A shows a representative 5 second epoch with order parameter plotted at the top, and Modes 1 and 2 plotted underneath. Null spikes are color-coded in black, while the stable periods are color-coded by the phase of Mode 1 (relative to an arbitrary reference sinusoid). Mode 1 phase was relatively constant during stable periods, but jumped sharply by up to 180° from one stable period to the next, across the intervening null spike. To visualize these Mode 1 phase jumps directly, we generated a “carry on” sinusoid for illustration purposes (thin black sinusoid in Fig. 5A), using the phase angle and instantaneous frequency of Mode 1 just prior to the onset of the null spike, which then “carried on" for the null spike duration to serve as a reference to visualize phase slip. This reveals that when Mode 1 reappeared following a null spike, it was typically completely out of phase from itself just prior to the null spike.

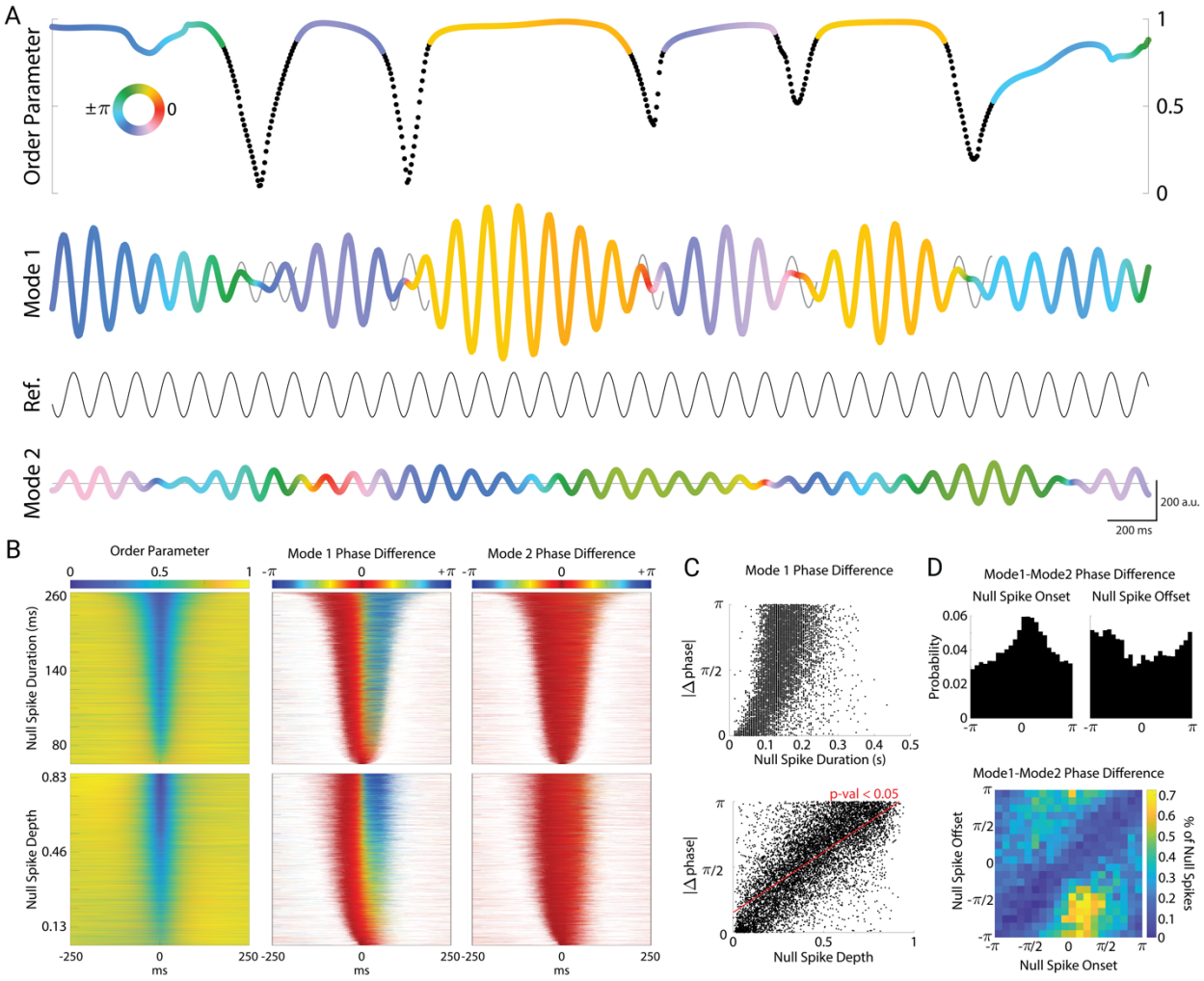

Figure 5. Cortical null spikes impose a phase-reset of Mode 1
(A) Example plot of null spikes and corresponding phase resets of Mode 1. Color of the order parameter and Mode 1 correspond to the phase angle between Mode 1 and a reference sinusoid set at the average frequency of Mode 1 (8.7 Hz). Black regions of the order parameter correspond to periods of a detected null spike. For each null spike, a "carry-on" signal is generated (gray sinusoids), representing the theoretical continuation of the mode at its instantaneous frequency immediately preceding the null spike. The color of Mode 2 corresponds to its own phase angle with the reference sinusoid. For simplicity, only the real components of the complex-valued modes are plotted (a.u.). **(B)** All null spikes (N = 9212) sorted by duration (top row) and depth (bottom row). Corresponding phase differences of Mode 1 (middle) and Mode 2 (right) with their respective carry-on signals plotted for each null spike. **(C)** Absolute value of change in phase plotted by null spike duration (top) and depth (bottom). Linear regression and p-value are plotted in red for null spike depth. **(D)** Distribution of phase differences between Mode 1 and Mode 2 at the onsets (top left) and offsets (top right) of the null spikes. Density plot of the onset angles with their corresponding offset angles (bottom).

In contrast, the phase of Mode 2 (Fig. 5A, bottom) varied smoothly and continuously and was unaffected by null spikes or stable periods. This was true across all null spikes and stable periods (Figure 5B). We sorted all null spikes by their duration (Figure 5B top left) to examine the phase slip of Mode 1 relative to the phase just prior to the onset of the null spike. The phase of Mode 1 jumped sharply at the midpoint of the null spike (Fig. 5B top middle), whereas the phase of Mode 2 remained stable across the duration of the null spike (Fig. 5B top right). When we instead sorted null spikes by their depth (peak-to-trough, Figure 5B bottom left), we observed that the magnitude of the Mode 1 phase jump during the null spike depended strongly on the depth of the null spike (Figure 5B bottom middle). That is, the deeper the null spike, the greater the phase jump across that null spike. Figure 5C shows the magnitude of the phase jump as a function of null spike duration (top) and null spike depth (bottom). While the magnitude of the phase reset showed a slight correlation with null spike duration, a strong correlation was found with null spike depth ($p < 0.05$).

Interestingly, null spikes tended to occur when Mode 1 and Mode 2 were nearly synchronized in phase. While the onset of null spikes occurred at various phase relationships between Mode 1 and Mode 2, there was a higher probability at a phase difference near zero (with a peak at $\pi/4$ radians), and a corresponding trough at the null spike offset (Figure 5D top). The joint probability distribution of these two measures shows the increased probability (in yellow) of null spike onsets to occur when Mode 1 and 2 were nearly synchronized (i.e. with a phase difference near zero). It also reveals the inverse relationship between Mode 1 and 2 at null spike offset (blue diagonal), because Mode 2 phase is stable across null spikes while Mode 1 phase inverts across null spikes. Thus, although only Mode 1 exhibits phase resets across null spikes (whereas Mode 2

does not), the phase angles of the two modes are not independent of one another, but rather tend to be in-phase at the onset of null spikes.

Discussion

We found that cortical theta oscillations are organized into distinct bilaterally-symmetric cortex-wide traveling waves. The dominant spatiotemporal pattern (Mode 1) was a divergent traveling wave originating in posterior retrosplenial cortex, and radiating rostrolaterally across the cortex in a bilaterally symmetric manner. Secondary modes of oscillation (Modes 2 and 3) were bilaterally symmetric spiral waves centered over somatosensory cortex. The rotational directions of Modes 2 and 3 were mirror-symmetric, and Mode 2 had high amplitude over medial frontal cortex whereas Mode 3 had high amplitude over the temporal poles. Mouse running speed was strongly correlated with mean theta amplitude, synchrony, and Mode 1 power. In contrast, other aspects of mouse behavior such as turning and movements of the ears and nose were unrelated to theta oscillations, even though these movements were correlated both with running speed and with each other. Theta oscillations showed metastable dynamics, in which stable periods of Mode 1 were punctuated by transient null spikes of low-amplitude asynchronous activity, during which Modes 2 and 3 were prominent. Moreover, these null spikes were associated with a phase reset of Mode 1. These brain-wide spatiotemporal patterns of theta oscillations could be involved in integrating sensory and motor information during natural behavior.

Volume conduction

To what extent could these cortical theta oscillations be attributed to volume conduction from hippocampal theta? There are at least 3 mechanisms that could generate the spatiotemporal patterns of theta oscillations in cortex, which are not mutually exclusive.

First, they could be produced by volume conduction from a hippocampal theta generator. This possibility is consistent with the spatial amplitude pattern of Mode 1, which is greatest over parietal cortex, where the dorsal aspect of CA1 is closest to the overlying cortex. The dependence of theta amplitude and synchrony on mouse speed is also consistent with a theta generator in the hippocampus, where theta shows a similar dependence on speed. Indeed, a previous report of widespread cortical theta oscillations concluded that it most likely arises by volume conduction from the hippocampus (Sirota *et al.*, 2008). (See also (Gerbrandt *et al.*, 1978; Kennedy *et al.*, 2023)). However, subsequent studies revealed that hippocampal theta oscillations are organized into a traveling wave along the septotemporal axis (Lubenov and Siapas, 2009; Patel *et al.*, 2012; Zhang and Jacobs, 2015). This direction of travel is orthogonal to the rostrolateral propagation of the Mode 1 traveling wave, which is therefore inconsistent with the possibility that Mode 1 is explained purely by volume conduction. The spatial amplitude patterns and spiral wave structures of Modes 2 and 3 are also inconsistent with volume conduction from the hippocampus, as are their lack of dependence on mouse speed.

A second possible mechanism that could underlie cortical theta oscillations is that the rhythm originates in the hippocampus, but that field potential oscillations are generated in cortex by synaptic input arising from widespread projections from the hippocampus to neocortex. In this scenario, cortical theta is hippocampally driven, but could exhibit a different spatiotemporal pattern due to transformation by hippocampal axonal projection patterns. This could explain the different directions of traveling waves in hippocampus and cortex, but cannot explain the existence of the additional spatiotemporal patterns exhibited by Modes 2 and 3.

Finally, a third possible mechanism that could underlie cortical theta oscillations is local

generation and propagation by intracortical circuitry, which could also be entrained by hippocampal input (Zold and Hussain Shuler, 2015). Because we did not have a depth electrode in the hippocampus, we cannot directly relate cortical theta oscillations to hippocampal theta. Our LFP recordings also lack cellular resolution, preventing us from linking these spatiotemporal motifs to spiking activity. Thus, our data cannot distinguish among the possible mechanisms described above, but based on the above considerations, our results seem most consistent with a combination of all three mechanisms.

Theta oscillations and traveling waves

In primates, theta oscillations coordinate large-scale cortical excitability, nested gamma oscillations, and mediate the rhythmic sampling of sustained attention (Lakatos *et al.*, 2009; Bahramisharif *et al.*, 2013; Helfrich *et al.*, 2018). In rodents, theta-modulated spiking across the cortex has similarly established theta as a temporal organizer of activity (Holsheimer, 1982; Muir and Bilkey, 1998; Hyman *et al.*, 2005; Siapas, Lubenov and Wilson, 2005; Hafting *et al.*, 2008; Sirota *et al.*, 2008; Fournier *et al.*, 2020). In contrast to synchrony, traveling waves have been hypothesized to allow some portion of the population to be responsive or optimally sensitive at any given time, and utilize distinct phase information to segment and categorize multiple inputs from each other and segment inputs from background (Ermentrout and Kleinfeld, 2001).

The spatial phase gradient of Mode 1 appears to resemble several patterns of neocortical organization observed across mammals. Mode 1 flows directly along the developmental expression gradients of Emx2 and Pax6, two highly conserved mammalian genes which regulate the arealization of the neocortex (Bishop, Goudreau and O'Leary, 2000). Additionally, this organization matches the principal gradient of functional connectivity observed in mice, which in

turn reflects the evolutionary origins of the neocortex (Huntenburg *et al.*, 2021). Lastly, Mode 1 is consistent with population analysis of traveling wave direction across the human cortex (Zhang *et al.*, 2018), and congruent with the dorsal and ventral streams of feed-forward processing (Goodale and Milner, 1992). More recent evidence shows that the directions of cortical traveling waves change dynamically across behavior, reflecting distinct states of neural processing (Mohan et al., 2024).

Metastability and phase resets

We found that theta oscillations occurred in bouts that lasted about 1 s, which were often punctuated by brief ~0.1 s periods of low amplitude and low synchrony, which we refer to as null spikes based on their similarity to previously described null spikes in gamma activity (Freeman, 2007; Kozma and Freeman, 2017). These findings are consistent with a growing number of reports of metastable dynamics, in which brain activity occurs as a sequence of discrete quasi-stationary states. Experimental and theoretical work has suggested that metastable states may underlie neural representations, with neural computation proceeding along a sequence of state transitions (La Camera, Fontanini and Mazzucato, 2019; Recanatesi *et al.*, 2022). Because our free exploration paradigm did not include an explicit task, we cannot relate the spatiotemporal motifs we observed to memory or perceptual representations. Nevertheless, our results suggest that metastable states may take the form of cortex-wide traveling waves, and that transitions appear to involve a phase reset in the dominant mode from one state to the next.

Phase resetting of ongoing oscillations modulate cortical excitability (Lakatos *et al.*, 2009), and are critical for coding strategies that rely on phase information (Canavier, 2015; Voloh and Womelsdorf, 2016). Spontaneous cortical waves have been shown to be phase-reset through visual

stimuli (Aggarwal *et al.*, 2024), and phase resets of hippocampal theta oscillations have been observed to occur during critical moments of behavioral sequences such as jumping in rodents (Green *et al.*, 2022), saccades in primates (Jutras, Fries and Buffalo, 2013), and working memory tasks in rats and humans (Givens, 1996; Tesche and Karhu, 2000). Here, we found that the magnitude of cortical null spikes was linearly related to phase resets of Mode 1. In other words, the amount of cortex-wide asynchrony during null spikes had a linear relationship to the resulting phase shift of the dominant cortical mode.

During these cortical null spikes, the ongoing spiral waves of Mode 2 remained stable, potentially suggesting it is generated independently from that of Mode 1. Additionally, because spiral waves inherently include all phases at any given point in time due to their circular nature, they impose asynchrony across the cortex. That is, synchrony (as measured by the order parameter) is low during null spikes because the relatively synchronous Mode 1 transiently weakens, leaving cortical theta dominated by asynchronous Modes 2 and 3.

The coupling of frontal cortex theta oscillations with the cortex-wide spiral waves of Mode 2 may reflect an important role in mediating communication between the hippocampus and neocortex. Previous observations of spiral wave dynamics have led to the suggestion that they may provide a means for the cortex to produce emergent ongoing oscillatory activity, as well as allow populations to disengage from globally-synchronous rhythms and produce a state change (Huang *et al.,* 2004; Huang *et al.*, 2010). The large-scale theta oscillations we describe here could be involved in the dynamic routing of information across widespread cortical areas. The integration of sensory and motor information during ongoing natural behavior requires a system for flexible communication among disparate cortical areas. Dynamic and metastable sequences of

spatiotemporal theta motifs could provide a substrate for such flexible communication.

CHAPTER IV

CONCLUSIONS

In this dissertation, I have presented new methodology to push the field of systems neuroscience forward, towards large-scale cortical recordings and comprehensive multisensory behavioral monitoring during natural behaviors in freely moving mice. Utilizing these methods, I identified novel patterns of mouse behavior and large-scale cortical activity.

In Chapter II, I presented a novel head-mounted camera system for monitoring freely moving mice. Because head-fixed conditions severely restrict the behavioral repertoire of animals and their willingness to engage in natural behaviors, recording neural activity and behavior in freely moving conditions is critical for studying the how the nervous system functions in behaviorally-relevant contexts. The ability to monitor the position and movements of the eyes, ears, nostrils, whiskers, and visual field in freely moving conditions therefore allows us to investigate how mice utilize their sensory systems in concert with one another to produce adaptive behaviors across a variety of ethological tasks. The flexibility of this system also allows for an incredibly wide range of configurations, enabling investigators to tailor the system to best fit their experimental goals.

Through the use of this system, I demonstrated its ability to capture the fine movements of these sensory organs across an array of diverse behaviors and custom implant fabrications. These included active behaviors such as prey capture, exploration, social behavior, and jumping, as well as behavior on longer scales such as sleep. Chronic monitoring across long timescales in this way also allows us to investigate the effects of arousal on stimulus processing across sensory

systems. Additionally, recording from freely moving mice in their home cage while utilizing this system to monitor their pupil value allows us to span much larger states of arousal than in head-fixed conditions.

The significant advantages in size, weight, and cabling, also allows simultaneous behavioral monitoring to be integrated with large-scale electrophysiological recordings. In Chapter II, I demonstrate its integration with tetrodes for single unit recordings and multi-channel wire-arrays for single channel recordings across many brain areas.

In Chapter III, I utilized this system to identify a tight link between mouse turning and the movements of their nose and ears in freely moving conditions, and expanded the design of multi-channel wire-array implants into brain-wide electrocorticography arrays to achieve simultaneous electrophysiological recordings across the neocortex. Because real-world behavior is inherently multisensory, and no brain area works in isolation, recording across many brain areas is critical for understanding how individual areas and populations of neurons function in the context of large-scale brain states.

Electrocorticography provides the proper spatial scale and temporal resolution necessary to monitor the cortex at large, and adequately resolve the natural rhythms the brain operates at. Theta oscillations (4-12 Hz) are preserved rhythm across mammals, and known to organize spiking activity across many brain areas for processes such as spatial navigation, sensorimotor integration, and memory formation and retrieval. I found that theta oscillations were prominent across the cortex, and spatiotemporally organized into three bilaterally-symmetric cortex-wide traveling waves which were strongly modulated by running speed. The dominant pattern (Mode 1) was a bilaterally-symmetric divergent traveling wave originating in retrosplenial cortex, while

Modes 2 and 3 were spiral waves centered over primary somatosensory cortex. Interestingly, Modes 2 and 3 exhibited opposite rotational directions, and while Mode 2 displayed a high amplitude in frontal cortex, Mode 3 displayed high amplitude in the temporal poles.

Similar to previous studies of spiking activity and gamma oscillations across species, these traveling waves showed metastable dynamics, alternating in prominence during transient desynchronization events (known as "null spikes"). Interestingly, these null spikes induced a phase reset in the dominant cortical mode, potentially suggesting that these transient desynchronization events allow for modes to dynamically realign their phase in time. Additionally, the stability of Mode 2 during these null spikes potentially suggests it is generated independently from that of Mode 1 and may reflect ongoing emergent activity of the neocortex.

Considering the significant role of theta in the hippocampus and other cortices, these brain-wide spatiotemporal patterns of theta oscillations may serve to similarly integrate multisensory information distributed across the entire cerebral cortex. Future studies should identify how these oscillations relate to traveling waves in other brain areas. The traveling waves described here provide the groundwork for future studies aimed at uncovering how multisensory spiking activity is assimilated across the cortex, and their potential role in adaptive behaviors.

APPENDIX 0

PARTS LIST

Part Number	Name	Source/Manufacturer	Part number or URL
1	LeeChatWin Analog Camera RS-306	AliExpress	link
2	Fusion 360	Autodesk	link
3	Cura	Ultimaker	link
4	Maker Select Plus 3D Printer	Monoprice	15711
5	Camera carrier	3D-print stl file	link
6	Video ground loop isolators	NewEgg	link
7	Loctite super glue	Loctite	1363589
8	30AWG Wrapping wire	NewEgg	link
9	Resistors	Amazon	link
10	Shrink tubing	Amazon	link
11	12 mm focal-length collimating lens	Lilly electronics	link
12	Fisher tape	Fisher Scientific	link
13	Micropore Surgical Tape	3M	70200412230
14	20G stainless-steel wire	Amazon	link
15	3 mm IR LED	Chanzon	100F3T-IR-FS-940NM
16	USB 2.0 Video Capture Card	UCEC	8541594679
17	Amplifier	Intan Technologies	#C3324 RHD 32ch + accel
18	RHD USB Interface Board	Intan Technologies	link
19	OpenEphys software		OpenEphys
20	Kilosort		Kilosort
21	Bonsai software		link
22	Webcam	ELP	ELP-USBFHD01M-BFV

PARTS LIST

23	IR dome USB camera	ELP	ELP-USBFHD05MT-DL36
24	Microphone	Brüel and Kjær	TYPE 4939-A-011
25	Lynx 22 sound card	Lynx	link
26	Audacity	Audacity	Audacity
27	Implant base	3D-print stl file	link
28	00-80	U-Turn Fasteners	link
29	18-8 washer	Amazon	B000FN1718
30	Teflon-coated stainless-steel wire	A&M Systems	791400
31	Small EIB pins	Neuralynx	link
32	EIB-36-PTB	Neuralynx	link
33	Tungsten wire (0.0007, Tungsten 99.95%, HFV insulation)	California Fine Wire Company	link
34	RTV silicone glue	Permatex	80050
35	EIB screws	Amazon	AMS90/8
36	Social cap	3D-print stl file	link
37	Skull screw	Grainger	2AE98
38	48 LED IR light source	Amazon	link
39	6000K LED Floodlight	Quans	Amazon
40	Clear plexiglass acrylic	ePlastics	ACRYCLR0.080FM48X72ACRYCLR0.080FM48X72
41	5500K 95+CRI light bulb	Litebox	HD-105

PARTS LIST

42	Adjustable IR LED light source	OSRAM	940nm LED Engin
43	Aluminum tape	Amazon	CECOMINOD062708
44	PTFE tape	Anti-Seize Technology	16030
45	Silver shielding paint	MG chemicals	842AR-15mL
46	Large EIB pins	Neuralynx	link
47	Electric connectors	Mill-Max	853-43-100-10-001000

APPENDIX 1

REMOVAL OF IR FILTER

Begin by unscrewing the lens located on the front of the camera (A). With the lens removed (B), place the camera out of the way and facedown on a clean surface to avoid any unwanted particles from accumulating on the sensor. Flip the lens over and begin using a scalpel blade around the edges of the filter to gently separate it from the lens. Once the filter has been sufficiently loosened around the edges, the blade will slide underneath it (C). Take care to avoid scratching the lens underneath during this process. Continue to work the blade around all sides of the filter until it can be fully removed from the lens (D). With the filter removed, screw the lens back onto the camera.

Test the video signal again using the camera's power and signal connectors, to confirm that the signal is now sensitive to an infrared light source and that the lens and sensor are free of any debris or damage that affects the video signal.

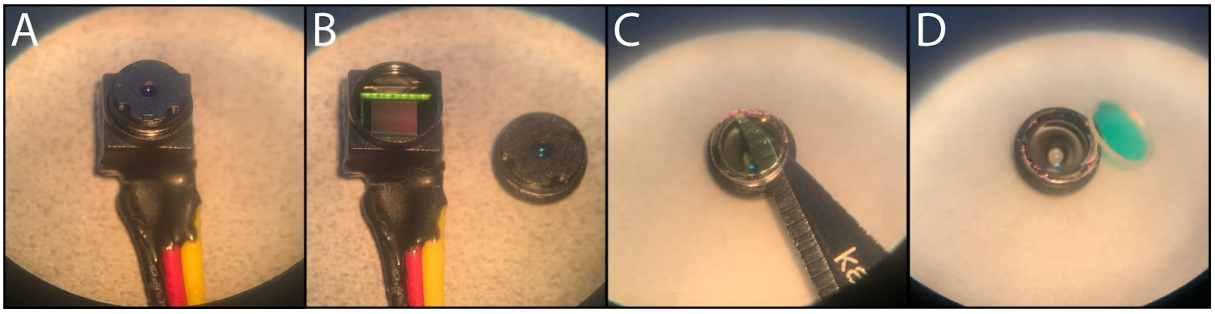

APPENDIX 2

CLEARING EXCESS RUBBER ADHESIVE

The cameras often come with a small amount of external rubber adhesive (an example is shown in A), which can interfere with positioning when placed into a camera carrier. To prevent irregular placement, we recommend that you ensure that the four sides of the camera are clear of any rubber adhesive around the square-shaped core of the module. Gently remove adhesive using a scalpel and forceps until all sides of the camera are clear (as in B).

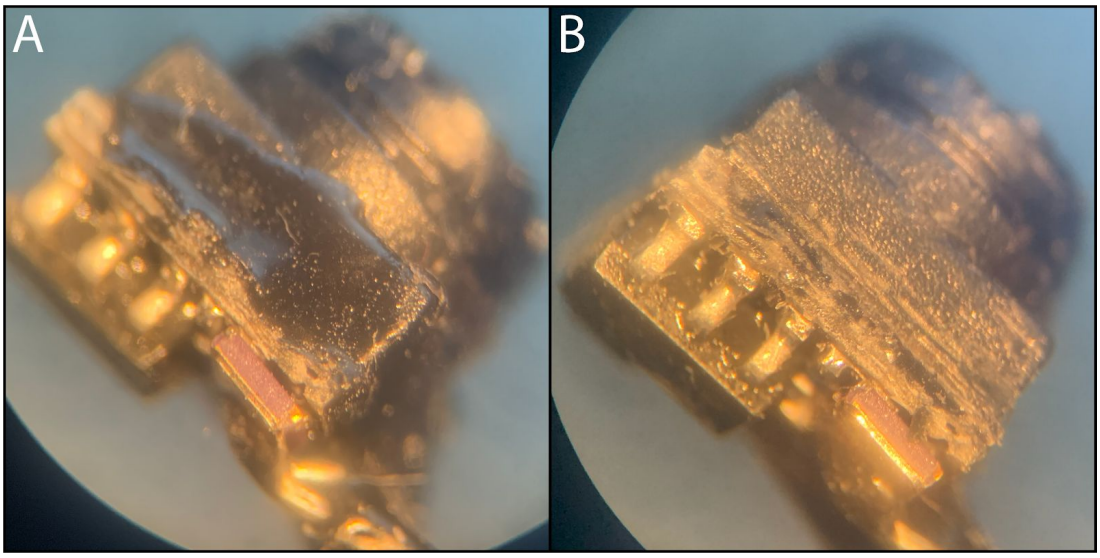

APPENDIX 3

STRIPPING THE CAMERA MODULE LEADS

Use wire cutters to cut the camera module's signal, power, and ground wires at least 5 mm from the camera modules. Then, using a scalpel blade and forceps, carefully strip the signal, power, and ground wires to the base of the camera module (B). Take care when stripping near the base of the module, and leave some excess rubber around their connections, so they are less likely to break from stress during assembly.

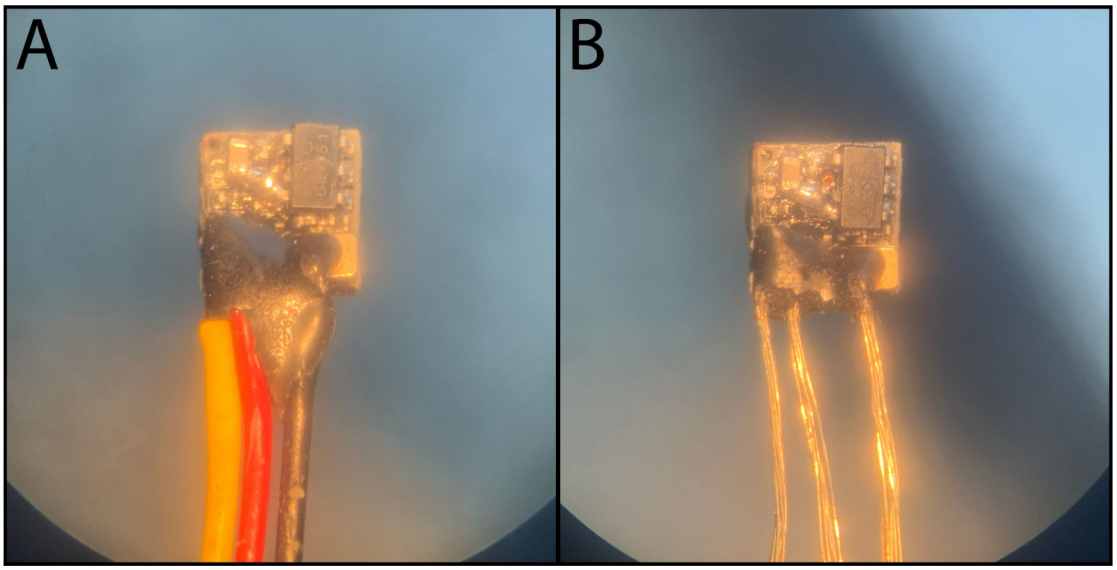

APPENDIX 4

PREPARING WIRE SEGMENTS FOR SOLDERING ONTO THE CAMERAS

Place the cameras in their appropriate holder on a carrier, with the accompanying LED(s) in place to use for reference while you prepare the wires that will power them. Strip and cut wires to the appropriate lengths, and solder on resistors where necessary (e.g. 390 **Ω**, Part #9). Panel A shows an example of power and ground wires customized for a four-camera headset, with specific gaps in insulation to solder to the cameras. Panel B shows an enlarged view of the power and ground wires for a right-ear camera. The signal wires for each camera (not pictured here) should be cut to be as long as your desired tether length.

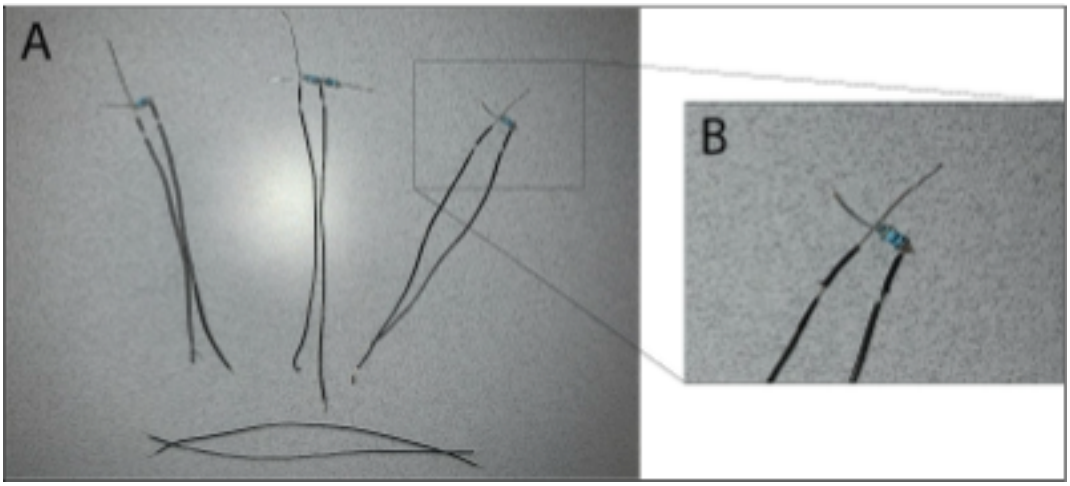

APPENDIX 5

SOLDERING THE WIRES ONTO THE CAMERAS AND INSULATING THEM WITH SILICONE GLUE

With a camera in its proper position on a carrier, solder the signal, power, and ground wires, so they are oriented in the proper direction towards the center of the carrier. This is shown for a left ear camera as an example in panels A, B, and C. Once soldered and trimmed, remove the camera from the carrier and coat the exposed wire with silicone glue (D) and allow it to dry, so they are fully insulated.

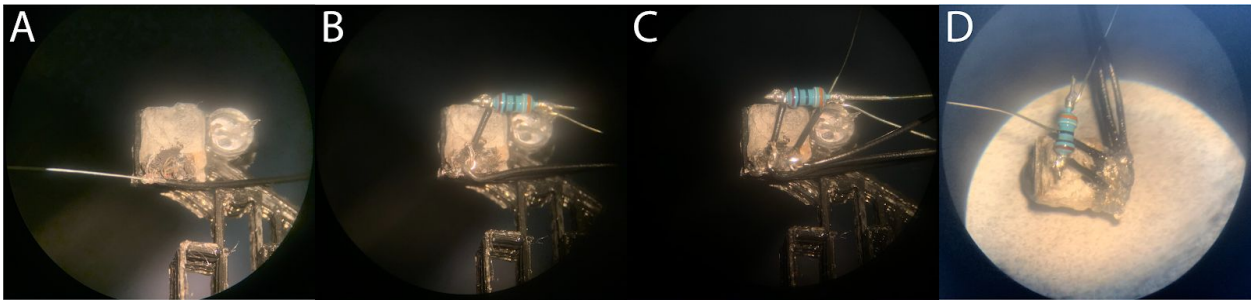

APPENDIX 6

SHIELDING, BENDING, WEAVING, AND STRIPPING THE WIRES

Close proximity of the wires and cameras to the headstage can introduce noise into the electrode channels. For this reason, we used aluminum tape to shield the electrical components of the headset. Cut a section of aluminum tape (Part #43) with a 5 mm wide strip running about 25 mm in length off of one side (A). Peel the backing from the strip, make two small cuts, and reinforce the joint with a small piece of tape or superglue to prevent tearing (A). Place the camera module at this joint, with the wires running on top of the strip (B). Wrap the strip around the three wires (C). Use a multimeter at this point to confirm that the aluminum is not electrically connected to any of the wires. Place the camera module in its proper position on a carrier and bend the wrapped wires at the proper locations so they feed towards the weaving lattice at the center of the carrier (D). Mark the location on the aluminum where the wires meet the first lattice crossbar on the carrier (shown by the red arrow in D). Remove the camera from the carrier, and peel back the aluminum strip to your marked location. Place the camera back on the carrier, and route the ends of the power and ground wires down through separate lattice windows of your choosing, and mark the location where they emerge from the bottom. It's recommended to route the power wires in separate windows from the ground wires so they are well-separated when they are eventually soldered to the tethers as described in Appendix 9. Remove the camera from the carrier, and strip the ends of the power and ground wires to where you made your mark. Repeat this for each camera while it is in its proper position.

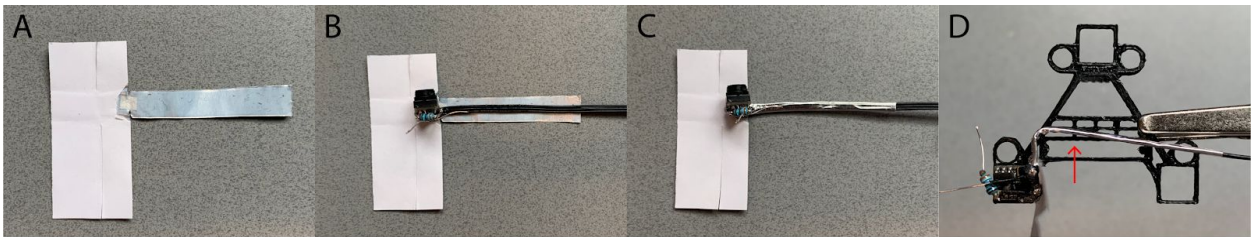

APPENDIX 7

CEMENTING THE CAMERAS ONTO THE CARRIER

Place the camera on the carrier with the power and ground wires in their proper windows, and weave the camera's signal tether down through a lattice window, and back up, so it emerges upward from the center of the carrier (A). Slightly remove the camera from its holder, apply a small amount of superglue gel around the sides, and place it back in its holder, ensuring that the surface of the camera is perfectly flush with the bottom surface of the camera carrier (B). Once the glue has completely cured and the camera is solidified into place, peel off the paper from the unapplied aluminum tape, and wrap the camera module so it is as completely encased as possible, adding silicone glue or PTFE tape (Part #44) between the aluminum and camera components for insulation as needed, to ensure they don't become electrically connected. Confirm this using a multimeter. Repeat these steps for the remaining cameras.

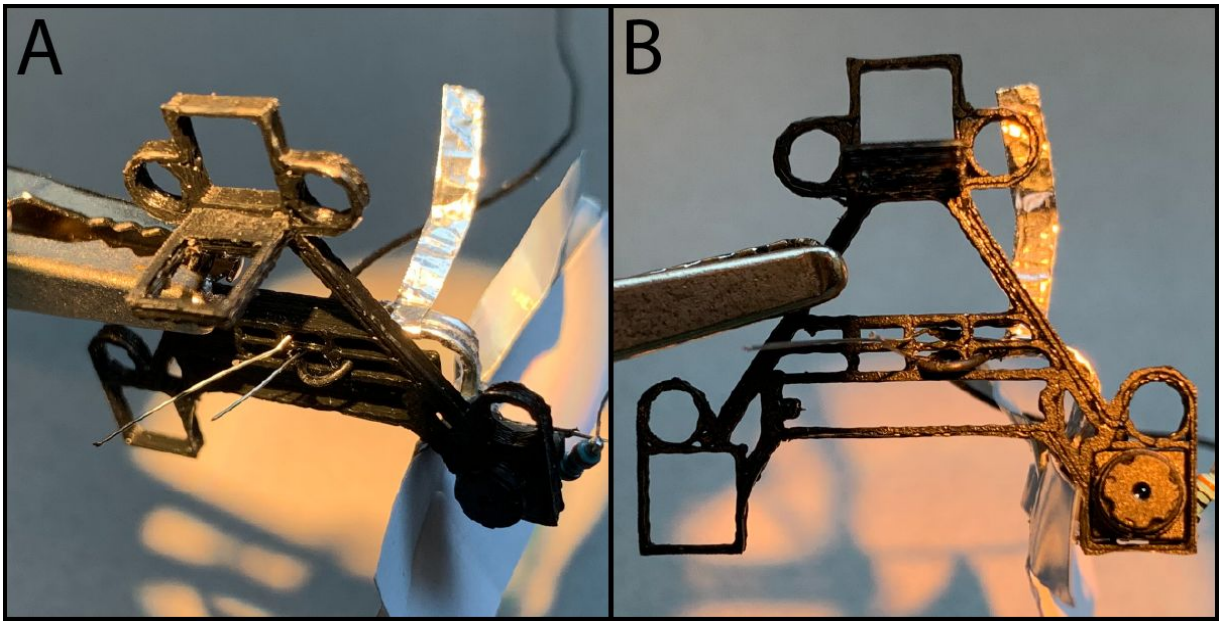

APPENDIX 8

ADDING THE LEDS

Trim the power and ground terminals of an IR LED, and insert it into an LED receiver on the carrier (shown by the black arrow in A). Wrap the local power and ground wires from the camera module to the leads of the LED (shown by the red and black arrows in B). Use a multimeter to ensure that no undesired connections to the shielding exist, and then solder them in place for a stable and permanent connection. Repeat these steps for the remaining LEDs.

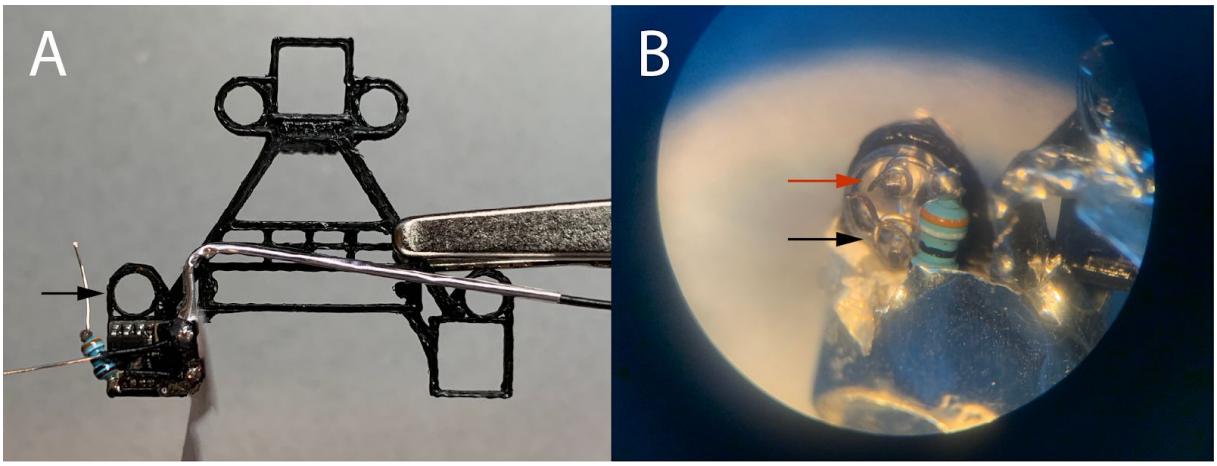

APPENDIX 9

SOLDERING THE POWER AND GROUND TETHERS

With all the cameras cemented in place and their power and ground wires extending from the bottom of the carrier (A), prepare two wires cut to your desired tether length to serve as the common power and ground tethers. Strip the ends of the wire, and feed it down through the appropriate window for the power or ground. Twist the 4 power (or ground) wires around the respective tether wire (B). Ensure that there is no connection between the power and ground wires using a multimeter. At this point, you should power the cameras to test that they all produce a proper video signal before moving forward. Solder the wrapped wires for a permanent connection, and completely cover this bare wire and solder with insulation so they can be wrapped with aluminum shielding in the next step.

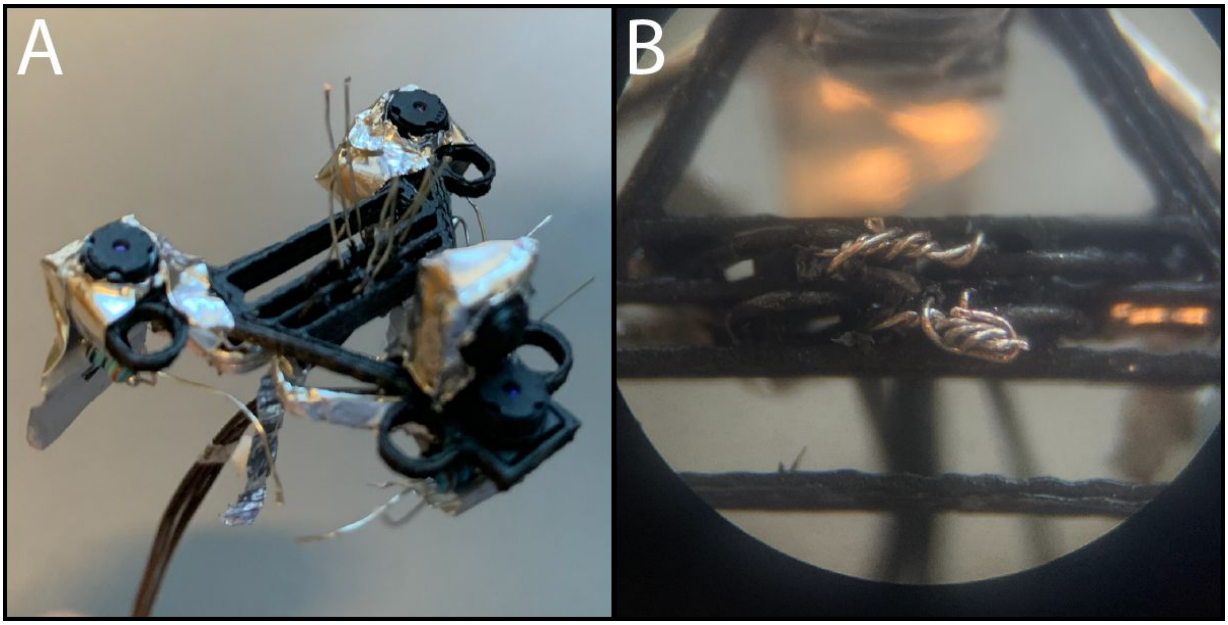

APPENDIX 10

SHIELDING THE WEAVING LATTICE AND INITIAL SEGMENT OF THE TETHERS

Cut a 75x15 mm piece of aluminum tape, with 2x1 mm notches on each side about 11 mm from the top (A). Peel and remove the backing from the top to the point of the notches (B). Replace the backing onto the aluminum, and fold the top portion as shown (B). For clarity, the next steps are shown with an empty carrier. Insert the top portion through the front opening, from the underside of the carrier (C). Remove the protective paper (D). Insert the remaining end through the front portion of the headstage window (E). Pull both sides upwards, so they surround the weaving lattice as shown (F). Press them together, so they encase the woven wires (G) and tethers (not shown). Trim and fold the remaining tape so the first 4cm of the tethers are completely encased, shown here on a prepared carrier (H). All shielding combined, as shown in (H), weighed 84 mg.

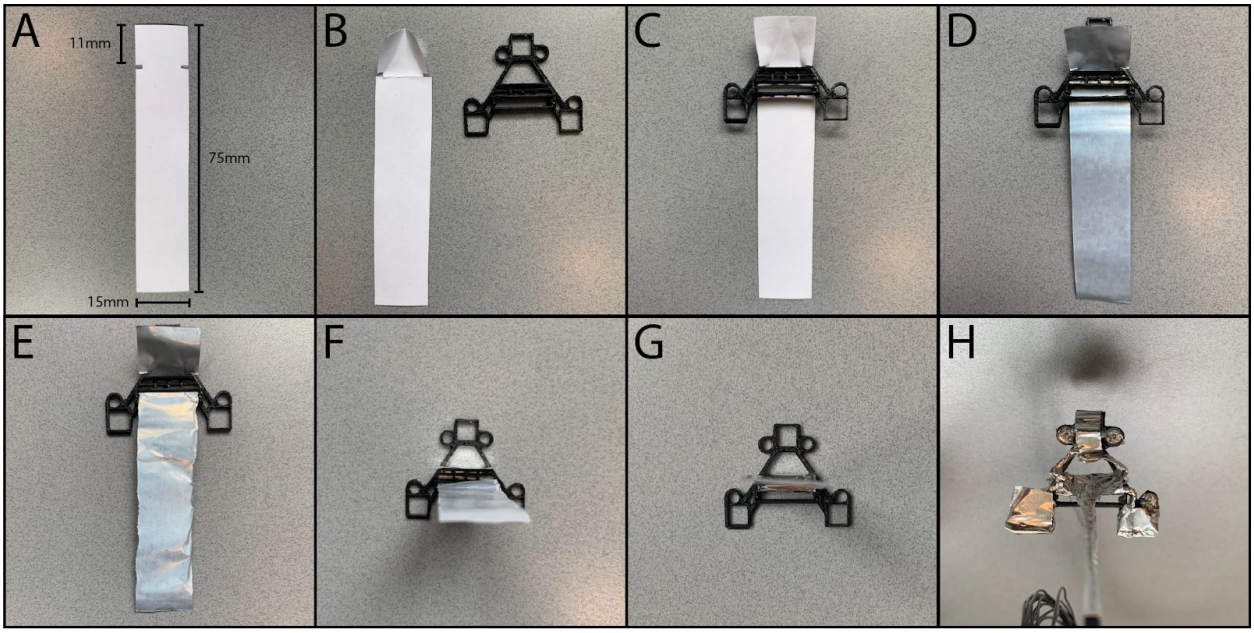

APPENDIX 11

ATTACHING THE HEADSET TO A HEADSTAGE

Unplug a headstage, and slide it up through the back of the headstage window on the headset with the front of the headstage facing forward, as seen with an empty carrier as an example in A. The fit is very tight, so we recommend practicing this on an empty carrier first to get an idea of how much force you'll need to use. Lower the headset until it reaches the bottom of the headstage as shown in B. Once placed on a headstage, the headset can be removed and reattached if necessary, but may cause wear and tear to the headset, and should be avoided.

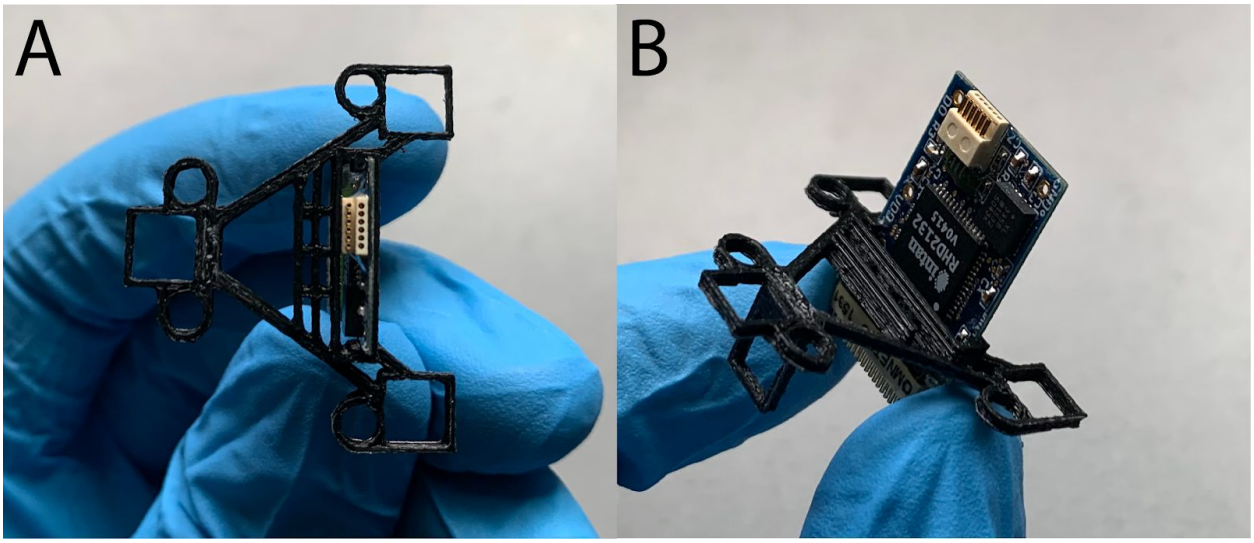

APPENDIX 12

GROUNDING THE SHIELDS

Prepare stripped wire to serve as the grounding connections for the shields. Create a small puncture in each of the aluminum shields of the headset, and weave the wire through them to create an electrical connection. Use a multimeter to confirm that all pieces of shielding have a low resistance connection to the remaining free end of the shielding wire. Use the multimeter once again to confirm that none of the shields have an electrical connection to any camera components at this point as well. Use silver conductive paint (Part #45) to adhere the shielding wire to the shielding tape at each connection point. Pin the free end of the shielding wire to either the GND or REF of the headstage with a large gold pin (Part #46), and coat it in silicone glue for a stable, yet removable connection. If pinning to REF, you'll need to shorten the length of the pin, and pin from the front of the headstage so it can make a solid connection without hitting the back of the carrier.

REFERENCES CITED

Chapter I

Lubenov, E.V. and Siapas, A.G. (2009) 'Hippocampal theta oscillations are travelling waves', *Nature*, 459(7246), pp. 534–539.

Patel, J. *et al.* (2012) 'Traveling theta waves along the entire septotemporal axis of the hippocampus', *Neuron*, 75(3), pp. 410–417.

Zhang, H. and Jacobs, J. (2015) 'Traveling Theta Waves in the Human Hippocampus', *The Journal of neuroscience: the official journal of the Society for Neuroscience*, 35(36), pp. 12477–12487.

Chapter II

Allen, L. M., Jayachandran, M., Viena, T. D., Su, M., McNaughton, B. L., and Allen, T. A. (2020). RatHat: a self-targeting printable brain implant system. *eNeuro* 7:ENEURO.0538-19.2020. doi: 10.1523/ENEURO.0538-19.2020

Angelaki, D. E., and Dickman, J. D. (2003). Premotor neurons encode torsional eye velocity during smooth-pursuit eye movements. *J. Neurosci.* 23, 2971–2979. doi: 10.1523/JNEUROSCI.23-07-02971.2003

Bagdasarian, K., Szwed, M., Knutsen, P. M., Deutsch, D., Derdikman, D., Pietr, M., et al. (2013). Pre-neuronal morphological processing of object location by individual whiskers. *Nat. Neurosci.* 16, 622–631. doi: 10.1038/nn.3378

Ballard, D. H. (1991). Animate vision. *Artif. Intell.* 48, 57–86. doi: 10.1016/0004-3702(91)90080-4

Benjamins, C. E., and Huizinga, E. (1929). Untersuchungen über die funktion des vestibularapparates bei der taube. *Pflügers Arch. Gesamte Physiol. Menschen Tiere* 221, 104–118. doi: 10.1007/BF01793968

Blumberg, M. S., Lesku, J. A., Libourel, P.-A., Schmidt, M. H., and Rattenborg, N. C. (2020). What is REM sleep? *Curr. Biol.* 30, R38–R49. doi: 10.1016/j.cub.2019.11.045

Carvell, G. E., and Simons, D. J. (1995). Task- and subject-related differences in sensorimotor behavior during active touch. *Somatosens. Mot. Res.* 12, 1–9.

Carvell, G. E., Simons, D. J., Lichtenstein, S. H., and Bryant, P. (1991). Electromyographic activity of mystacial pad musculature during whisking behavior in the rat. *Somatosens. Mot. Res.* 8, 159–164. doi: 10.3109/08990229109144740

Cooper, M. L., and Pettigrew, J. D. (1979). A neurophysiological determination of the vertical horopter in the cat and owl. *J. Comp. Neurol.* 184, 1–26. doi: 10.1002/cne.901840102

Crawford, J. D., Cadera, W., and Vilis, T. (1991). Generation of torsional and vertical eye position signals by the interstitial nucleus of cajal. *Science* 252, 1551–1553. doi: 10.1126/science.2047862

Datta, S. R., Anderson, D. J., Branson, K., Perona, P., and Leifer, A. (2019). Computational neuroethology: a call to action. *Neuron* 104, 11–24. doi: 10.1016/j.neuron.2019.09.038

Felius, J., Locke, K. G., Hussein, M. A., Stager, D. R. Jr, and Stager, D. R. Sr. (2009). Photographic assessment of changes in torsional strabismus. *J. AAPOS* 13, 593–595. doi: 10.1016/j.jaapos.2009.09.008

Gibson, J. J. (1962). Observations on active touch. *Psychol. Rev.* 69, 477–491. doi: 10.1037/h0046962

Helmholtz, H. (1925). *Treatise on Physiological Optics*. Rochester, NY: Optical Society of America.

Holland, R. A., and Waters, D. A. (2005). Echolocation signals and pinnae movement in the fruitbat rousettus aegyptiacus. *Acta Chiropt.* 7, 83–90. doi: 10.3161/1733-5329(2005)7[83:ESAPMI]2.0.CO;2

Hoshino, S., Takahashi, R., Mieno, K., Tamatsu, Y., Azechi, H., Ide, K., et al. (2020). The reconfigurable maze provides flexible, scalable, reproducible, and repeatable tests. *iScience* 23:100787. doi: 10.1016/j.isci.2019.100787

Hoy, J. L., Yavorska, I., Wehr, M., and Niell, C. M. (2016). Vision drives accurate approach behavior during prey capture in laboratory mice. *Curr. Biol.* 26, 3046–3052. doi: 10.1016/j.cub.2016.09.009

Lederman, S. J., and Klatzky, R. L. (1987). Hand movements: a window into haptic object recognition. *Cogn. Psychol.* 19, 342–368. doi: 10.1016/0010-0285(87)90008-9

Mainland, J., and Sobel, N. (2006). The sniff is part of the olfactory percept. *Chem. Senses.* 31, 181–196. doi: 10.1093/chemse/bjj012

Mathis, A., Mamidanna, P., Cury, K. M., Abe, T., Murthy, V. N., Mathis, M. W., et al. (2018). DeepLabCut: markerless pose estimation of user-defined body parts with deep learning. *Nat. Neurosci.* 21, 1281–1289. doi: 10.1038/s41593-018-0209-y

Matthis, J. S., Yates, J. L., and Hayhoe, M. M. (2018). Gaze and the control of foot placement when walking in natural terrain. *Curr. Biol.* 28, 1224–1233.e5. doi: 10.1016/j.cub.2018.03.008

Meyer, A. F., Poort, J., O'Keefe, J., Sahani, M., and Linden, J. F. (2018). A head-mounted camera system integrates detailed behavioral monitoring with multichannel electrophysiology in freely moving mice. *Neuron* 100, 46–60.e7. doi: 10.1016/j.neuron.2018.09.020

Michaiel, A.M. (2019), *Dynamic Visual Processing: Creating Representations of the World*, Doctoral Dissertation. University of Oregon. ProQuest Dissertations Publishing (27545881)

Michaiel, A. M., Abe, E. T. T., and Niell, C. M. (2020). Dynamics of gaze control during prey capture in freely moving mice. *Elife* 9:e57458. doi: 10.7554/eLife.57458.sa2

Musall, S., Kaufman, M. T., Juavinett, A. L., Gluf, S., and Churchland, A. K. (2019). Single-trial neural dynamics are dominated by richly varied movements. *Nat. Neurosci.* 22, 1677–1686. doi: 10.1038/s41593-019-0502-4

Musall, S., Kaufman, M. T., Gluf, S., and Churchland, A. K. (2018). Movement-related activity dominates cortex during sensory-guided decision making. *bioRxiv.* Available online at: https://www.biorxiv.org/content/10.1101/308288v2.abstract (accessed December 14, 2020).

O'Regan, J. K., and Noë, A. (2001). A sensorimotor account of vision and visual consciousness. *Behav. Brain Sci.* 24, 939–973. doi: 10.1017/S0140525X01000115

Pachitariu, M., Steinmetz, N. A., Kadir, S. N., Carandini, M., and Harris, K. D. (2016). Fast and accurate spike sorting of high-channel count probes with kilosort. *Adv. Neural Inf. Process. Syst.* 29, 4448–4456. doi: 10.5555/3157382.3157595

Parker, P. R., Brown, M. A., Smear, M. C., and Niell, C. M. (2020). Movement-related signals in sensory areas: roles in natural behavior. *Trends Neurosci.* 43, 581–595. doi: 10.1016/j.tins.2020.05.005

Parsa, C. F., and Kumar, A. B. (2013). Cyclodeviation of the retinal vascular arcades: an accessory sign of ocular torsion. *Br. J. Ophthalmol.* 97, 126–129. doi: 10.1136/bjophthalmol-2011-300867

Populin, L. C., and Yin, T. C. (1998). Pinna movements of the cat during sound localization. *J. Neurosci.* 18, 4233–4243. doi: 10.1523/JNEUROSCI.18-11-04233.1998

Preyer, W. (1882). *Die Seele des Kindes.* Leipzig: Grieben-Verlag. Robinson, D. A. (1963). A method of measuring eye movement using a scleral search coil in a magnetic field. IEEE Trans. Bio Med. Electron. 10, 137–145. doi: 10.1109/TBMEL.1963.4322822

Salkoff, D. B., Zagha, E., McCarthy, E., and McCormick, D. A. (2020). Movement and performance explain widespread cortical activity in a visual detection task. *Cereb. Cortex* 30, 421–437. doi: 10.1093/cercor/bhz206

Sattler, N., and Wehr, M. (2020). A head-mounted multi-camera system for electrophysiology and behavior in freely-moving mice. *bioRxiv* [Preprint]. doi: 10.1101/2020.06.30.181412

Saunders, J. L., and Wehr, M. (2019). Autopilot: automating behavioral experiments with lots of raspberry pis. *bioRxiv* [Preprint]. doi: 10.1101/807693

Schwarz, J. S., Sridharan, D., and Knudsen, E. I. (2013). Magnetic tracking of eye position in freely behaving chickens. *Front. Syst. Neurosci.* 7:91. doi: 10.3389/fnsys.2013.00091

Shen, E. P., Chen, W.-L., and Hu, F.-R. (2010). Manual limbal markings versus iris-registration software for correction of myopic astigmatism by laser in situ keratomileusis. *J. Cataract Refract. Surg.* 36, 431–436. doi: 10.1016/j.jcrs.2009.10.030

Steinmetz, N. A., Aydin, C., Lebedeva, A., Okun, M., Pachitariu, M., Bauza, M., et al. (2020). Neuropixels 2.0: a miniaturized high-density probe for stable, long-term brain recordings. *Cold Spring Harbor Laboratory.* Available online at: https://www.biorxiv.org/content/10.1101/2020.10.27.358291v1.abstract (accessed November 28, 2020).

Sterratt, D. C., Lyngholm, D., Willshaw, D. J., and Thompson, I. D. (2013). Standard anatomical and visual space for the mouse retina: computational reconstruction and transformation of flattened retinae with the retistruct package. *PLoS Computat. Biol.* 9:e1002921. doi: 10.1371/journal.pcbi.1002921

Stringer, C., Pachitariu, M., Steinmetz, N., Reddy, C. B., Carandini, M., and Harris, K. D. (2019). Spontaneous behaviors drive multidimensional, brainwide activity. *Science* 364:255. doi: 10.1126/science.aav7893

Tollin, D. J., Ruhland, J. L., and Yin, T. C. T. (2009). The vestibulo-auricular reflex. *J. Neurophysiol.* 101, 1258–1266. doi: 10.1152/jn.90977.2008

Tweed, D., and Vilis, T. (1987). Implications of rotational kinematics for the oculomotor system in three dimensions. *J. Neurophysiol.* 58, 832–849. doi: 10.1152/jn.1987.58.4.832

Voigts, J., Siegle, J. H., Pritchett, D. L., and Moore, C. I. (2013). The flexDrive: an ultra-light implant for optical control and highly parallel chronic recording of neuronal ensembles in freely moving mice. *Front. Syst. Neurosci.* 7:8. doi: 10.3389/fnsys.2013.00008

Volland, S., Esteve-Rudd, J., Hoo, J., Yee, C., and Williams, D. S. (2015). A comparison of some organizational characteristics of the mouse central retina and the human macula. *PLoS ONE* 10:e0125631. doi: 10.1371/journal.pone.0125631

Wallace, D. J., Greenberg, D. S., Sawinski, J., Rulla, S., Notaro, G., and Kerr, J. N. D. (2013). Rats maintain an overhead binocular field at the expense of constant fusion. *Nature* 498, 65–69. doi: 10.1038/nature12153

Welker, W. I. (1964). Analysis of sniffing of the albino rat 1. *Behaviour* 22, 223–244. doi: 10.1163/156853964X00030

Wells, W. C. (1794). Reply to Dr. darwin on vision. *Gentleman's Mag. Histor. Chron.* 64, 905–907.

Yüzgeç, Ö., Prsa, M., Zimmermann, R., and Huber, D. (2018). Pupil size coupling to cortical states protects the stability of deep sleep via parasympathetic modulation. *Curr. Biol.* 28, 392–400.e3. doi: 10.1016/j.cub.2017.12.049

Chapter III

Abeles, M. *et al.* (1995) 'Cortical activity flips among quasi-stationary states', *Proceedings of the National Academy of Sciences of the United States of America*, 92(19), pp. 8616–8620.

Aggarwal, A. *et al.* (2024) 'Neural assemblies coordinated by cortical waves are associated with waking and hallucinatory brain states', *Cell reports*, 43(4), p. 114017.

Bahramisharif, A. *et al.* (2013) 'Propagating neocortical gamma bursts are coordinated by traveling alpha waves', *The Journal of neuroscience: the official journal of the Society for Neuroscience*, 33(48), pp. 18849–18854.

Benchenane, K. *et al.* (2010) 'Coherent theta oscillations and reorganization of spike timing in the hippocampal- prefrontal network upon learning', *Neuron*, 66(6), pp. 921–936.

Bishop, K.M., Goudreau, G. and O'Leary, D.D. (2000) 'Regulation of area identity in the mammalian neocortex by Emx2 and Pax6', *Science*, 288(5464), pp. 344–349.

Buzsáki, G. (2002) 'Theta oscillations in the hippocampus', *Neuron*, 33(3), pp. 325–340.

Cabral, J. *et al.* (2022) 'Metastable oscillatory modes emerge from synchronization in the brain spacetime connectome', *Communications Physics*, 5(1), pp. 1–13.

Canavier, C.C. (2015) 'Phase-resetting as a tool of information transmission', *Current opinion in neurobiology*, 31, pp. 206–213.

Ermentrout, G.B. and Kleinfeld, D. (2001) 'Traveling electrical waves in cortex: insights from phase dynamics and speculation on a computational role', *Neuron*, 29(1), pp. 33–44.

Fournier, J. *et al.* (2020) 'Mouse Visual Cortex Is Modulated by Distance Traveled and by Theta Oscillations', *Current biology: CB*, 30(19), pp. 3811–3817.e6.

Freeman, W.J. (2007) 'Proposed Cortical "Shutter" Mechanism in Cinematographic Perception', in L.I. Perlovsky and R. Kozma (eds) *Neurodynamics of Cognition and Consciousness*. Berlin, Heidelberg: Springer Berlin Heidelberg, pp. 11–38.

Fries, P. (2005) 'A mechanism for cognitive dynamics: neuronal communication through neuronal coherence', *Trends in cognitive sciences*, 9(10), pp. 474–480.

Gerbrandt, L.K. *et al.* (1978) 'Origin of the neocortically monitored theta rhythm in the curarized rat', *Electroencephalography and clinical neurophysiology*, 45(4), pp. 454–467.

Givens, B. (1996) 'Stimulus-evoked resetting of the dentate theta rhythm: relation to working memory', *Neuroreport*, 8(1), pp. 159–163.

Goodale, M.A. and Milner, A.D. (1992) 'Separate visual pathways for perception and action', *Trends in neurosciences*, 15(1), pp. 20–25.

Green, L. *et al.* (2022) 'Action-driven remapping of hippocampal neuronal populations in jumping rats', *Proceedings of the National Academy of Sciences of the United States of America*, 119(26), p. e2122141119.

Hafting, T. *et al.* (2008) 'Hippocampus-independent phase precession in entorhinal grid cells', *Nature*, 453(7199), pp. 1248–1252.

Helfrich, R.F. *et al.* (2018) 'Neural Mechanisms of Sustained Attention Are Rhythmic', *Neuron*, 99(4), pp. 854–865.e5.

Holsheimer, J. (1982) 'Generation of theta activity (RSA) in the cingulate cortex of the rat', *Experimental brain research. Experimentelle Hirnforschung. Experimentation cerebrale*, 47(2), pp. 309–312.

Huang, X. *et al.* (2004) 'Spiral waves in disinhibited mammalian neocortex', *The Journal of neuroscience: the official journal of the Society for Neuroscience*, 24(44), pp. 9897–9902.

Huang, X. *et al.* (2010) 'Spiral wave dynamics in neocortex', *Neuron*, 68(5), pp. 978–990.

Huntenburg, J.M. *et al.* (2021) 'Gradients of functional connectivity in the mouse cortex reflect neocortical evolution', *NeuroImage*, 225, p. 117528.

Hyman, J.M. *et al.* (2005) 'Medial prefrontal cortex cells show dynamic modulation with the hippocampal theta rhythm dependent on behavior', *Hippocampus*, 15(6), pp. 739–749.

Jones, L.M. *et al.* (2007) 'Natural stimuli evoke dynamic sequences of states in sensory cortical ensembles', *Proceedings of the National Academy of Sciences of the United States of America*, 104(47), pp. 18772–18777.

Jones, M.W. and Wilson, M.A. (2005a) 'Phase precession of medial prefrontal cortical activity relative to the hippocampal theta rhythm', *Hippocampus*, 15(7), pp. 867–873.

Jones, M.W. and Wilson, M.A. (2005b) 'Theta rhythms coordinate hippocampal-prefrontal interactions in a spatial memory task', *PLoS biology*, 3(12), p. e402.

Jutras, M.J., Fries, P. and Buffalo, E.A. (2013) 'Oscillatory activity in the monkey hippocampus during visual exploration and memory formation', *Proceedings of the National Academy of Sciences of the United States of America*, 110(32), pp. 13144–13149.

Kennedy, J.P. *et al.* (2023) 'Visual cortical LFP in relation to the hippocampal theta rhythm in track running rats', *Frontiers in cellular neuroscience*, 17, p. 1144260.

Kim, J., Delcasso, S. and Lee, I. (2011) 'Neural correlates of object-in-place learning in hippocampus and prefrontal cortex', *The Journal of neuroscience: the official journal of the Society for Neuroscience*, 31(47), pp. 16991–17006.

Kozma, R. and Freeman, W.J. (2008) 'Intermittent spatio-temporal desynchronization and sequenced synchrony in ECoG signals', *Chaos*, 18(3), p. 037131.

Kozma, R. and Freeman, W.J. (2017) 'Cinematic Operation of the Cerebral Cortex Interpreted via Critical Transitions in Self-Organized Dynamic Systems', *Frontiers in systems neuroscience*, 11, p. 10.

La Camera, G., Fontanini, A. and Mazzucato, L. (2019) 'Cortical computations via metastable activity', *Current opinion in neurobiology*, 58, pp. 37–45.

Lakatos, P. *et al.* (2009) 'The leading sense: supramodal control of neurophysiological context by attention', *Neuron*, 64(3), pp. 419–430.

Lubenov, E.V. and Siapas, A.G. (2009) 'Hippocampal theta oscillations are travelling waves', *Nature*, 459(7246), pp. 534–539.

M Aghajan, Z. *et al.* (2017) 'Theta Oscillations in the Human Medial Temporal Lobe during Real-World Ambulatory Movement', *Current biology: CB*, 27(24), pp. 3743–3751.e3.

Mathis, A. *et al.* (2018) 'DeepLabCut: markerless pose estimation of user-defined body parts with deep learning', *Nature neuroscience*, 21(9), pp. 1281–1289.

Mégevand, P. *et al.* (2008) 'A mouse model for studying large-scale neuronal networks using EEG mapping techniques', *NeuroImage*, 42(2), pp. 591–602.

Mohan, U.R., Zhang, H., Ermentrout, B. and Jacobs, J. (2024). 'The direction of theta and alpha travelling waves modulates human memory processing.' *Nature Human Behaviour*, [online] pp.1–12. doi:https://doi.org/10.1038/s41562-024-01838-3.

Muir, G.M. and Bilkey, D.K. (1998) 'Synchronous modulation of perirhinal cortex neuronal activity during cholinergically mediated (type II) hippocampal theta', *Hippocampus*, 8(5), pp. 526–532.

Musall, S. *et al.* (2019) 'Single-trial neural dynamics are dominated by richly varied movements', *Nature neuroscience*, 22(10), pp. 1677–1686.

Parker, P.R. *et al.* (2020) 'Movement-Related Signals in Sensory Areas: Roles in Natural Behavior', *Trends in neurosciences*, in press.

Patel, J. *et al.* (2012) 'Traveling theta waves along the entire septotemporal axis of the hippocampus', *Neuron*, 75(3), pp. 410–417.

Ponce-Alvarez, A. *et al.* (2012) 'Dynamics of cortical neuronal ensembles transit from decision making to storage for later report', *The Journal of neuroscience: the official journal of the Society for Neuroscience*, 32(35), pp. 11956–11969.

Recanatesi, S. *et al.* (2022) 'Metastable attractors explain the variable timing of stable behavioral action sequences', *Neuron*, 110(1), pp. 139–153.e9.

Roberts, J.A. *et al.* (2019) 'Metastable brain waves', *Nature communications*, 10(1), p. 1056.

Sattler, N.J. and Wehr, M. (2021) 'A Head-Mounted Multi-Camera System for Electrophysiology and Behavior in Freely-Moving Mice', *Frontiers in Neuroscience*, 14, p. 592417.

Schneider, D.M. and Mooney, R. (2018) 'How Movement Modulates Hearing', *Annual review of neuroscience*, 41, pp. 553–572.

Siapas, A.G., Lubenov, E.V. and Wilson, M.A. (2005) 'Prefrontal phase locking to hippocampal theta oscillations', *Neuron*, 46(1), pp. 141–151.

Siegle, J.H. *et al.* (2017) 'Open Ephys: an open-source, plugin-based platform for multichannel electrophysiology', *Journal of neural engineering*, 14(4), p. 045003.

Sirota, A. *et al.* (2008) 'Entrainment of neocortical neurons and gamma oscillations by the hippocampal theta rhythm', *Neuron*, 60(4), pp. 683–697.

Stringer, C. *et al.* (2019) 'Spontaneous behaviors drive multidimensional, brainwide activity', *Science*, 364(6437), p. 255.

Tesche, C.D. and Karhu, J. (2000) 'Theta oscillations index human hippocampal activation during a working memory task', *Proceedings of the National Academy of Sciences of the United States of America*, 97(2), pp. 919–924.

Voloh, B. and Womelsdorf, T. (2016) 'A Role of Phase-Resetting in Coordinating Large Scale Neural Networks During Attention and Goal-Directed Behavior', *Frontiers in systems neuroscience*, 10, p. 18.

Xu, Y. *et al.* (2023) 'Interacting spiral wave patterns underlie complex brain dynamics and are related to cognitive processing', *Nature human behaviour*, 7(7), pp. 1196–1215.

Zhang, H. *et al.* (2018) 'Theta and Alpha Oscillations Are Traveling Waves in the Human Neocortex', *Neuron*, 98(6), pp. 1269–1281.e4.

Zhang, H. and Jacobs, J. (2015) ‘Traveling Theta Waves in the Human Hippocampus’, *The Journal of neuroscience: the official journal of the Society for Neuroscience*, 35(36), pp. 12477–12487.

Zold, C.L. and Hussain Shuler, M.G. (2015) ‘Theta Oscillations in Visual Cortex Emerge with Experience to Convey Expected Reward Time and Experienced Reward Rate’, *The Journal of neuroscience: the official journal of the Society for Neuroscience*, 35(26), pp. 9603–9614.